Novel quadratic Bézier triangular and tetrahedral elements using existing mesh generators: Extension to nearly incompressible implicit and explicit elastodynamics in finite strains

C. Kadapa
Swansea Academy of Advanced Computing,
Swansea University, Bay Campus, Swansea SA1 8EN, Wales, UK.
(c.kadapa@swansea.ac.uk)

Abstract

We present a novel unified finite element framework for performing computationally efficient large strain implicit and explicit elastodynamic simulations using triangular and tetrahedral meshes that can be generated using the existing mesh generators. For the development of a unified framework, we use Bézier triangular and tetrahedral elements which are directly amenable for explicit schemes using lumped mass matrices, and employ a mixed displacement-pressure formulation for dealing with the numerical issues arising due to volumetric and shear locking. We demonstrate the accuracy of the proposed scheme by studying several challenging benchmark problems in finite strain elastostatics and nonlinear elastodynamics modelled with nearly incompressible hyperelastic and von Mises elastoplastic material models. We show that Bézier elements, in combination with the mixed formulation, help in developing a simple unified finite element formulation that is accurate, robust and computationally very efficient for performing a wide variety of challenging nonlinear elastostatic and implicit and explicit elastodynamic simulations.

1 Introduction

Finite element method (FEM) has been a highly successful numerical scheme for the computer simulation of solid mechanics problems over the past few decades. Today, FEM is one of the well-established numerical techniques with a strong mathematical foundation and a plethora of open-source and commercial software suites with simulation capabilities for a wide range of solid and fluid mechanics problems. Among the various schemes in the paradigm of finite element methods, those based on the triangular and tetrahedral elements receive considerable attention from the simulation engineers. This interest is because of the ease of mesh generation with triangular and tetrahedral elements even for highly intricate and complex real-world geometries. The ease of mesh generation with triangular/tetrahedral elements has driven the development of many numerical techniques for performing simulations using these elements. While numerous established finite element schemes that are accurate and efficient in overcoming volumetric-locking and shear-locking using implicit formulations are available today, such schemes are still a scarcity for explicit dynamic simulations which find many useful applications in Engineering. Few such applications are impact and crashworthiness simulations in the transportation industry, simulation of manufacturing processes such as deep drawing in the manufacturing industry and complex geomechanics simulations in geotechnical engineering.

Notwithstanding the tremendous amount of research that gone into the development of finite element techniques for the simulation of complex engineering problems, unified finite element formulations that are accurate, robust and computationally efficient, and, more importantly, that are applicable for elastostatic and implicit elastodynamic as well as explicit elastodynamic simulations of problems modelled with nearly incompressible hyperelastic and elastoplastic material models, are still lacking. This deficiency is mainly due to a few disadvantages of triangular/tetrahedral Lagrange elements that limit their applicability to explicit elastodynamic simulations consisting of nearly incompressible elastic and elastoplastic material models. These disadvantages are:

- Despite their straightforward applicability to explicit schemes, the performance of linear triangular/tetrahedral Lagrange elements is quite poor, even for compressible materials, using the pure displacement formulation, and they are practically useless for nearly incompressible and elastoplastic material models.

- Although higher-order Lagrange elements are less prone to *volumetric-* and *shear-locking*, they pose serious issues when used with the explicit schemes.

To overcome the above-discussed issues and perform accurate numerical simulations using explicit schemes with triangular/tetrahedral meshes, various numerical schemes have been proposed over the past few decades. The discussion of all such numerical schemes is beyond the scope of the present work. We discuss only some important contributions and refer the reader to the references therein for further details.

Some notable contributions towards finite element schemes for performing the simulations of problems modelled with nearly incompressible and elastoplastic material models using triangular/tetrahedral elements are: fractional-step based projection schemes by Zienkiewicz and collaborators [1]; averaged nodal pressure approach by Bonet et al. [2]; node-based uniform strain elements by Dohrmann et al. [3]; stabilised nodally integrated elements by Puso and Solberg [4]; smoothed finite element method by Liu et al. [5]; F-bar patch for triangular and tetrahedral elements by de Souza Neto et al. [6]; 15-node tetrahedral element with reduced-order integration by Danielson [7]; mean-strain 10-node tetrahedral with energy-sampling stabilisation by Pakravan et al. [8, 9]; discontinuous Galerkin methods by Hansbo and Larson [10], Noels and Radovitzky [11] and Nguyen and Peraire [12]; mixed-stabilised formulations for solid mechanics problems by by Franca et al. [13], Maniatty and collaborators [14, 15, 16], Masud and Xia [17, 18], Chiumenti and Cervera group [19, 20, 21, 22] and Scovazzi et al. [23, 24, 25, 26, 27]; and schemes based on first-order conservation laws by Bonet, Gil and co-workers [28, 29].

Even though the above-discussed schemes address the difficulties in modelling nearly incompressible materials to varying degrees of success, they do pose certain limitations in developing a unified finite element framework that is accurate, robust and computationally efficient for performing elastostatic and implicit elastodynamic as well as explicit elastodynamic simulations. The author believes that this deficiency is mainly due to the long-lasting reliance of the majority of the finite element schemes on the Lagrange family of elements which, due to some inherent disadvantages, do not offer a suitable framework for the development of unified finite element formulations. Although the discontinuous Galerkin methods offer a suitable framework for the explicit schemes, the introduction of additional solution variables, for example, deformation gradient or stress, together with the computational cost incurred for the storage and the inversion of element-wise consistent mass matrices, makes these schemes computationally less attractive for large-scale simulations. Furthermore, higher-order Lagrange elements pose additional numerical difficulties for contact-impact problems.

Towards addressing the issues associated with modelling nearly incompressible material models using triangular and tetrahedral elements, especially, for explicit elastodynamics, and developing unified finite element formulations, we have recently proposed a novel finite element framework by adapting the Bernstein polynomials from the paradigm of isogeometric analysis, see [30], and exploiting the existing mesh generators for the Lagrange elements. In Kadapa [31], we have extended the $\mathbf{B}$-bar formulation to quadratic Bézier triangular/tetrahedral elements and demonstrated that the combination of the $\mathbf{B}$-bar formulation and Bézier elements yields a unified framework for elastostatic and implicit and explicit elastodynamics. In [31], we have also proposed mapping techniques for generating the finite element meshes with Bézier elements from the corresponding Lagrange elements. The present work is the extension of our previous effort [31] to solid mechanics problems in finite strains. In particular, we focus on nearly incompressible Neo-Hookean hyperelastic models and finite strain von Mises elastoplasticity.

In this work, we adopt the mixed displacement-pressure formulation which has been studied extensively for solid mechanics problems, see [32, 33, 34]. In particular, in this work, we approximate the displacement field using quadratic Bernstein polynomials and the pressure field either as an element-wise discontinuous function or a linear Bernstein polynomials. These displacement-pressure combinations are tantamount to the P2/P0 and P2/P1 elements in the finite element literature. By studying several challenging benchmark examples, we demonstrate that this simple finite element framework is sufficient enough for performing accurate and computationally efficient elastostatic as well as implicit and explicit elastodynamic simulations of problems modelled with nearly incompressible hyperelastic and von Mises elastoplastic material models. It is worth pointing out that the proposed work, especially, the explicit scheme, is not limited to quadratic Bézier elements; it is also applicable for any suitable displacement-pressure combinations for which mass matrices can be approximated as lumped mass matrices. Quadratic Bézier elements are used in this work because of the ease of mesh generation by exploiting the existing mesh generators.

The outline of the paper is as follows. The governing equations and the finite element formulations used in the present work are discussed in Section 2. First, the accuracy of the proposed work is assessed by studying several elastostatic benchmark examples in Section 3. Later, the proposed scheme is applied to study several challenging benchmark examples in nonlinear elastodynamics in Section 4. The paper is concluded with Section 5 with a summary of the observations made and conclusions drawn.

2 Finite element formulation for finite strains

The finite element formulations used in the present work are already well established in the finite element literature. Therefore, we present only the important aspects of the formulations and refer the reader to any of the standards textbooks on nonlinear finite element analysis, for example, Zienkiewicz and Taylor [32] or Bathe [35] or de Souza Neto et al. [36] or Bonet and Wood [37], for the comprehensive details.

2.1 Governing equations

Consider an arbitrary solid body with Ω as its reference configuration. Under the influence of external forces, the body assumes a new configuration, say ω. The new configuration can be represented with a mapping $\boldsymbol{\phi} : \Omega \to \omega$ that takes a point $\mathbf{X} \in \Omega$ to a point $\mathbf{x} \in \omega$. Following this, the new configuration, ω, can be identified by a displacement field from the initial configuration, Ω. The displacement field is defined as

$$\boldsymbol{u}(\mathbf{X}) := \boldsymbol{\phi}(\mathbf{X}) - \mathbf{X} = \mathbf{x} - \mathbf{X}. \tag{1}$$

Now, using the definition of the displacement field in (1), and for a given strain energy function W, several important strain and stress measures for the finite strain continuum mechanics are defined as

$$\text{Deformation gradient,} \quad \mathbf{F} := \frac{\partial \mathbf{x}}{\partial \mathbf{X}} = \mathbf{I} + \frac{\partial \mathbf{u}}{\partial \mathbf{X}}, \tag{2}$$

$$\text{Right Cauchy-Green deformation tensor,} \quad \mathbf{C} := \mathbf{F}^{\mathrm{T}}\mathbf{F}, \tag{3}$$

$$\text{Left Cauchy-Green deformation tensor,} \quad \mathbf{b} := \mathbf{F}\mathbf{F}^{\mathrm{T}}, \tag{4}$$

$$\text{Green-Lagrange strain tensor,} \quad \mathbf{E} := \frac{1}{2}\left(\mathbf{C} - \mathbf{I}\right), \tag{5}$$

$$\text{Determinant of deformation gradient,} \quad J := \det(\mathbf{F}), \tag{6}$$

$$\text{First Piola-Kirchhoff stress tensor,} \quad \mathbf{P} := \frac{\partial W}{\partial \mathbf{F}} = \mathbf{F}\,\mathbf{S}, \tag{7}$$

$$\text{Second Piola-Kirchhoff stress tensor,} \quad \mathbf{S} := 2\frac{\partial W}{\partial \mathbf{C}} = \frac{\partial W}{\partial \mathbf{E}}, \tag{8}$$

$$\text{Cauchy stress tensor,} \quad \boldsymbol{\sigma} := \frac{1}{J}\,\mathbf{F}\,\mathbf{S}\,\mathbf{F}^{\mathrm{T}}. \tag{9}$$

Following the above definitions, the equations governing the elastodynamics in the finite strain regime, in the original configuration, are

$$\rho_0(\mathbf{X},t)\,\boldsymbol{a}(\mathbf{X},t) - \nabla^{\mathrm{X}} \cdot \mathbf{P}(\mathbf{X},t) = \mathbf{f}_0(\mathbf{X},t) \qquad \forall\, \mathbf{X} \in \Omega, t \in [0,T] \tag{10a}$$

$$\boldsymbol{u}(\mathbf{x},t) = \mathbf{g}_0(\mathbf{X},t) \qquad \forall\, \mathbf{X} \in \Gamma_{\mathrm{D}}, t \in [0,T] \tag{10b}$$

$$\mathbf{P}(\mathbf{X},t) \cdot \mathbf{N} = \mathbf{t}_0(\mathbf{X},t) \qquad \forall\, \mathbf{X} \in \Gamma_{\mathrm{N}}, t \in [0,T] \tag{10c}$$

$$\boldsymbol{u}(\mathbf{X},0) = \boldsymbol{u}_0(\mathbf{X}) \qquad \forall\, \mathbf{X} \in \Omega \tag{10d}$$

$$\boldsymbol{v}(\mathbf{X},0) = \boldsymbol{v}_0(\mathbf{X}) \qquad \forall\, \mathbf{X} \in \Omega \tag{10e}$$

where T is the total time span; ρ_0 is initial the density of the solid; $\boldsymbol{u}$ is the displacement vector; $\boldsymbol{v}(= \frac{d\boldsymbol{u}}{dt})$ is the velocity vector; $\boldsymbol{a}(= \frac{d^2\boldsymbol{u}}{dt^2})$ is the acceleration vector; $\boldsymbol{u}_0$ is the initial displacement vector; $\boldsymbol{v}_0$ is the initial velocity vector; $\mathbf{N}$ is the unit outward normal on the boundary, Γ, of Ω; $\mathbf{f}_0$ is body force in the initial configuration; $\mathbf{g}_0$ is prescribed displacement field on the Dirichlet boundary Γ_{D}; and $\mathbf{t}_0$ is the prescribed traction forces on the Neumann boundary Γ_{N}. The Dirichlet and Neumann boundaries are such that $\Gamma = \Gamma_{\mathrm{D}} \cup \Gamma_{\mathrm{N}}$ and $\Gamma_{\mathrm{D}} \cap \Gamma_{\mathrm{N}} = \emptyset$.

2.2 Displacement formulation

For a given stored energy function, W, the total energy functional, Π, in the reference configuration, Ω, is given by

$$\Pi(\boldsymbol{u}) = \int_{\Omega} W(\mathbf{C})\, \mathrm{d}\Omega \;-\; \Pi_{\mathrm{ext}} \tag{11}$$

where Π_{ext} is the energy contribution from the body and traction forces. Π_{ext} is given as

$$\Pi_{\mathrm{ext}} = \int_{\Omega} \boldsymbol{u}^{\mathrm{T}}\mathbf{f}_0\, \mathrm{d}\Omega + \int_{\Gamma_{\mathrm{N}}} \boldsymbol{u}^{\mathrm{T}}\,\mathbf{t}_0\, \mathrm{d}\Gamma \tag{12}$$

Following the principle of variation and taking approximations for the displacement field, $\boldsymbol{u}$, as

$$\boldsymbol{u} = \mathbf{N}_u \mathbf{u}, \tag{13}$$

the semi-discrete equations for displacement formulation may be written as

$$\mathbf{M}_{uu}\, \boldsymbol{a} + \mathbf{F}^{\text{int,disp}} = \mathbf{F}^{\text{ext}}, \tag{14}$$

where the mass matrix, $\mathbf{M}_{uu}$, the vector of external forces, $\mathbf{F}^{\text{ext}}$, and the vector of internal forces, $\mathbf{F}^{\text{int,disp}}$, are given by

$$\mathbf{M}_{uu} = \int_{\Omega} \rho_0\, \mathbf{N}_u^{\mathrm{T}}\, \mathbf{N}_u \, \mathrm{d}\Omega, \tag{15}$$

$$\mathbf{F}^{\text{int,disp}} = \int_{\omega} \mathbf{B}^{\mathrm{T}}\, \boldsymbol{\sigma} \, \mathrm{d}\omega, \tag{16}$$

$$\mathbf{F}^{\text{ext}} = \int_{\Omega} \mathbf{N}_u^{\mathrm{T}}\, \mathbf{f}_0 \, \mathrm{d}\Omega + \int_{\Gamma_{\mathrm{N}}} \mathbf{N}_u^{\mathrm{T}}\, \mathbf{t}_0 \, \mathrm{d}\Gamma. \tag{17}$$

The semi-discrete equations for the displacement formulation in equation (14) can now be solved in time using either explicit or implicit time integration schemes as discussed in the following subsections.

2.2.1 Implicit time integration

To obtain the implicit solutions in the present work, the generalised-α scheme of Kadapa et al. [38] is used. Following [38], we get

$$\mathbf{M}_{uu}\, \mathbf{a}_{n+\alpha_m} + \mathbf{F}^{\text{int,disp}}(\mathbf{u}_{n+\alpha_f}) = \mathbf{F}^{\text{ext}}_{n+\alpha_f} \tag{18}$$

where,

$$\mathbf{a}_{n+\alpha_m} = \alpha_m\, \mathbf{a}_{n+1} + (1-\alpha_m)\, \mathbf{a}_n \tag{19}$$

$$\mathbf{u}_{n+\alpha_f} = \alpha_f\, \mathbf{u}_{n+1} + (1-\alpha_f)\, \mathbf{u}_n \tag{20}$$

$$\mathbf{F}^{\text{ext}}_{n+\alpha_f} = \alpha_f\, \mathbf{F}^{\text{ext}}_{n+1} + (1-\alpha_f)\, \mathbf{F}^{\text{ext}}_{n} \tag{21}$$

$$\mathbf{v}_{n+1} = \frac{\alpha_m}{\alpha_f \gamma \Delta t}\, (\mathbf{u}_{n+1} - \mathbf{u}_n) + \frac{(\alpha_f - 1)}{\alpha_f} \mathbf{v}_n + \frac{(\gamma - \alpha_m)}{\gamma \alpha_f}\, \dot{\mathbf{u}}_n \tag{22}$$

$$\mathbf{a}_{n+1} = \frac{\alpha_m}{\alpha_f \gamma^2 \Delta t^2}\, (\mathbf{u}_{n+1} - \mathbf{u}_n) - \frac{1}{\alpha_f \gamma \Delta t}\, \mathbf{v}_n + \frac{\gamma - 1}{\gamma}\, \mathbf{a}_n + \frac{(\gamma - \alpha_m)}{\alpha_f \gamma^2 \Delta t}\, \dot{\mathbf{u}}_n \tag{23}$$

$$\dot{\mathbf{u}}_{n+1} = \frac{1}{\gamma \Delta t}\, (\mathbf{u}_{n+1} - \mathbf{u}_n) + \frac{\gamma - 1}{\gamma}\, \dot{\mathbf{u}}_n \tag{24}$$

and

$$\mathbf{F}^{\text{ext}}_{(\cdot)} = \int_{\Omega} \mathbf{N}_u^{\mathrm{T}}\, \mathbf{f}_{0(\cdot)} \, \mathrm{d}\Omega + \int_{\Gamma_{\mathrm{N}}} \mathbf{N}_u^{\mathrm{T}}\, \mathbf{t}_{0(\cdot)} \, \mathrm{d}\Gamma. \tag{25}$$

The parameters α_f, α_m and γ must be computed as

$$\alpha_f = \frac{1}{1+\rho_\infty}; \quad \alpha_m = \frac{3-\rho_\infty}{2(1+\rho_\infty)}; \quad \gamma = \frac{1}{2} + \alpha_m - \alpha_f; \quad \text{for} \quad 0 \leq \rho_\infty \leq 1, \tag{26}$$

such that the time integration scheme is unconditionally stable and second-order accurate. For further details on the characteristics of the scheme, we refer the reader to [38].

At this point, it is to be pointed out that the implicit scheme considered in this work is only second-order in time while the convergence rate of the displacement field for the quadratic elements is third-order accurate in space. This, however, is neither a disadvantage nor a limitation of the proposed work. To achieve equal-order accuracy in space and time, the time integration scheme can be replaced with the backward differentiation formula with the third-order accuracy, popularly known as the BDF3 scheme.

Using the Newton-Raphson scheme to solve the set of nonlinear equations (18), we get

$$\mathbf{K}^{\text{disp}}_{uu}\, \Delta \mathbf{u} = -\mathbf{R}^{\text{disp}}_{u}, \tag{27}$$

where $\mathbf{K}_{uu}^{\text{disp}}$ is the effective stiffness matrix, $\mathbf{R}_u^{\text{disp}}$ is the residual and $\Delta\mathbf{u}$ is the incremental displacement, at iteration $k+1$. Assuming deformation-independent loads, the effective stiffness matrix and the residual are given as

$$\mathbf{K}_{uu}^{\text{disp}} = \frac{\alpha_m^2}{\alpha_f \gamma^2 \Delta t^2}\,\mathbf{M}_{uu} + \alpha_f \mathbf{K}_{\text{M}} + \alpha_f \mathbf{K}_{\text{G}}, \tag{28}$$

$$\mathbf{R}_u^{\text{disp}} = \mathbf{M}_{uu}\,\mathbf{a}_{n+\alpha_m}^k + \mathbf{F}^{\text{int,disp}}(\mathbf{u}_{n+\alpha_f}^k) - \mathbf{F}_{n+\alpha_f}^{\text{ext}}. \tag{29}$$

Here, $\mathbf{K}_{\text{M}}$ and $\mathbf{K}_{\text{G}}$ are the material stiffness and geometric stiffness matrices, respectively, and are given as

$$\mathbf{K}_{\text{M}} = \int_\omega \mathbf{B}^{\text{T}}\mathbf{D}\mathbf{B}\,\mathrm{d}\omega \quad \text{and} \quad \mathbf{K}_{\text{G}} = \int_\omega \mathbf{G}^{\text{T}}\mathbf{\Sigma}\mathbf{G}\,\mathrm{d}\omega, \tag{30}$$

where $\mathbf{B}$ and $\mathbf{G}$ are the strain-displacement and gradient-displacement matrices with respect to the current configuration, and $\mathbf{\Sigma}$ is a fourth-order tensor that is defined as a function of the Cauchy stress as, $\Sigma_{ijkl} = \sigma_{jl}\delta_{ik}$. The nodal DOF values $\mathbf{u}_{n+\alpha_f}^k$ and $\mathbf{a}_{n+\alpha_m}^k$ are computed using the relations

$$\mathbf{u}_{n+\alpha_f}^k = \alpha_f\,\mathbf{u}_{n+1}^k + (1-\alpha_f)\,\mathbf{u}_n, \tag{31}$$

$$\mathbf{a}_{n+\alpha_m}^k = \alpha_m\,\mathbf{a}_{n+1}^k + (1-\alpha_m)\,\mathbf{a}_n. \tag{32}$$

2.2.2 Explicit time integration

By adapting the explicit scheme of [39] to the semi-discrete equation (14), we get

$$\mathbf{M}_{uu}\,\mathbf{a}_{n+1} = \mathbf{F}_n^{\text{ext}} - \mathbf{F}^{\text{int, disp}}(\mathbf{u}_n) \tag{33a}$$

$$\mathbf{u}_{n+1} = \mathbf{u}_n + \Delta t\,\mathbf{v}_n + \Delta t^2\left[\left(\frac{1}{2}-\beta\right)\mathbf{a}_n + \beta\,\mathbf{a}_{n+1}\right] \tag{33b}$$

$$\mathbf{v}_{n+1} = \mathbf{v}_n + \Delta t\left[(1-\gamma)\,\mathbf{a}_n + \gamma\,\mathbf{a}_{n+1}\right]. \tag{33c}$$

Following [31], the parameters are chosen as $\gamma = 3/2$ and $\beta = \frac{13}{12}$ such that scheme is *third-order accurate* in time for the undamped linear spring-mass system, and for the efficient solution of the equation (33a) the lumped-mass matrices are used. Using the row-sum-lumping technique, the lumped-mass matrices for the quadratic Bézier triangular and tetrahedral elements become

$$\mathbf{M}^{e,\text{tria}} = \frac{\rho\,V_0^e}{6}\quad \text{diag}[\mathbf{1}_6 \quad \mathbf{1}_6] \tag{34}$$

$$\mathbf{M}^{e,\text{tetra}} = \frac{\rho\,V_0^e}{10}\quad \text{diag}[\mathbf{1}_{10} \quad \mathbf{1}_{10} \quad \mathbf{1}_{10}] \tag{35}$$

where V_0^e is the volume of the element in the original configuration, $\mathbf{1}_6 = [1 \quad 1 \quad 1 \quad 1 \quad 1 \quad 1]$ and $\mathbf{1}_{10} = [1 \quad 1 \quad 1 \quad 1 \quad 1 \quad 1 \quad 1 \quad 1 \quad 1 \quad 1]$. It is important to mention at this point that the mass matrices used for the implicit scheme are the consistent mass matrices, unless specified otherwise. However, for the sake of brevity, the global mass matrix in both the implicit and explicit schemes is represented as $\mathbf{M}_{uu}$.

2.3 Two-field mixed formulation

For modelling nearly incompressible material models in finite strains, the deformation gradient, $\mathbf{F}$, is decomposed into deviatoric and volumetric components as

$$\mathbf{F} = \mathbf{F}_{\text{vol}}\,\mathbf{F}_{\text{dev}}; \quad \text{with} \quad \mathbf{F}_{\text{vol}} := J^{1/3}\mathbf{I}, \quad \text{and} \quad \mathbf{F}_{\text{dev}} := J^{-1/3}\mathbf{F}. \tag{36}$$

Using the above definitions, modified stress and strain measures are defined as

$$\text{Modified deformation gradient,} \quad \overline{\mathbf{F}} := J^{-1/3}\,\mathbf{F} \tag{37}$$

$$\text{Modified right Cauchy-Green deformation tensor,} \quad \overline{\mathbf{C}} := \overline{\mathbf{F}}^{\text{T}}\,\overline{\mathbf{F}} \tag{38}$$

$$\text{Modified left Cauchy-Green deformation tensor,} \quad \overline{\mathbf{b}} := \overline{\mathbf{F}}\,\overline{\mathbf{F}}^{\text{T}} \tag{39}$$

$$\text{Modified Green-Lagrange strain tensor,} \quad \overline{\mathbf{E}} := \frac{1}{2}\left(\overline{\mathbf{C}} - \mathbf{I}\right) \tag{40}$$

$$\text{Modified second Piola-Kirchhoff stress tensor,} \quad \overline{\mathbf{S}} := \partial W(\overline{\mathbf{E}})/\partial\overline{\mathbf{E}} \tag{41}$$

For the purpose of mixed formulation, we define the Cauchy stress tensor as

$$\widehat{\boldsymbol{\sigma}}(\boldsymbol{u}, p) = \overline{\boldsymbol{\sigma}}_{\mathrm{dev}}(\boldsymbol{u}) + p\,\mathbf{m} \tag{42}$$

where

$$\overline{\boldsymbol{\sigma}}_{\mathrm{dev}}(\boldsymbol{u}) = \overline{\boldsymbol{\sigma}}(\boldsymbol{u}) - \overline{p}\,\mathbf{m} \tag{43}$$

with

$$\overline{p} = \frac{1}{3}\mathbf{m}^{\mathrm{T}}\overline{\boldsymbol{\sigma}}(\boldsymbol{u}) \quad \text{and} \quad \mathbf{m} = \begin{bmatrix} 1 & 1 & 1 & 0 & 0 & 0 \end{bmatrix}^{\mathrm{T}}, \tag{44}$$

and p is the hydrostatic pressure which, for nearly incompressible material models in finite strains, is given by

$$p = \frac{\partial U}{\partial J}, \tag{45}$$

where $U = U(J)$ is the volumetric energy function. For all the material models considered in this work, the stored energy function, W, is assumed to be split into deviatoric part, $\overline{W}(J, \overline{C})$, and volumetric part, $U(J)$, as

$$W = \overline{W}(J, \overline{C}) + U(J). \tag{46}$$

Now, considering displacement, $\boldsymbol{u}$ and pressure, p, as independent variables, and taking their approximations as

$$\boldsymbol{u} = \mathbf{N}_u\,\mathbf{u} \quad \text{and} \quad p = \mathbf{N}_p\,\mathbf{p}, \tag{47}$$

the semi-discrete equations for the mixed formulation may be written as

$$\mathbf{M}_{uu}\,\mathbf{a} + \mathbf{F}^{\text{int,mixed}} = \mathbf{F}^{\text{ext}}, \tag{48a}$$

$$\mathbf{R}_p = \mathbf{0}, \tag{48b}$$

where the vector of internal forces, $\mathbf{F}^{\text{int,mixed}}$, and the residual of pressure equation (45), $\mathbf{R}_p$, are given by

$$\mathbf{F}^{\text{int,mixed}} = \int_{\omega} \mathbf{B}^{\mathrm{T}}\,\widehat{\boldsymbol{\sigma}}\;\mathrm{d}\omega, \tag{49}$$

$$\mathbf{R}_p = \int_{\Omega} \frac{1}{\kappa}\,\mathbf{N}_p^{\mathrm{T}}\left(\frac{\partial U}{\partial J} - p\right)\;\mathrm{d}\Omega. \tag{50}$$

2.3.1 Displacement-pressure combinations — accuracy and inf-sup stability

It is now an established fact that for the mixed displacement-pressure formulation, the combination of approximation spaces for the displacement and pressure fields should be chosen such that they satisfy the *inf-sup* stability condition. In the Lagrange family of elements, Taylor-Hood elements are the widely used *inf-sup* stable elements. For comprehensive details on *inf-sup* stability and the commonly used inf-sup stable elements for solid mechanics problems, we refer the reader to [32, 35, 40, 41]. Despite the widespread use of Taylor-Hood elements for elastostatic and implicit elastodynamic schemes, they are not ideally suited for explicit dynamic simulations due to the obvious difficulties posed by the higher order Lagrange elements for explicit schemes. Therefore, in this work, we use Bézier triangular and tetrahedral elements which are proven to be well suited for explicit schemes, see [31]. Following the established wisdom on inf-sup stable elements for solid mechanics problems, we can choose quadratic Bernstein functions for the displacement field and either linear or constant basis functions for the pressure field, resulting in the combinations BT2/BT1 and BT2/BT0, with BT0, BT1 and BT2 referring to the constant, linear and quadratic Bézier triangular or tetrahedral elements.

The inf-sup stability characteristics and spatial convergence rates of these combinations are illustrated, respectively, in Figures 1 and 2 using numerical examples with manufactured solutions. The inf-sup constants are evaluated by following the numerical procedure outlined in Chapelle and Bathe [42], and the error norms are evaluated using the mixed displacement-pressure formulation in small-strain studied previously in [33, 34]. From these graphs, it can be observed that

- The combination BT2/BT1 is not only inf-sup stable in both two and three dimensions but also converges with superoptimal convergence rates in the displacement as well as stress fields.

- The combination BT2/BT0 is inf-sup stable in 2D but not in 3D. Moreover, for the 2D problem, the convergence rates obtained with the combination BT2/BT0 are one order lower than those of the combination BT2/BT1, and the convergence rates become even worse for the 3D problem.

These observations are consistent with the characteristics of corresponding Lagrange elements, P2/P0 and P2/P1, presented in the literature on mixed elements, for example, Brezzi and Fortin and [41] Gmeiner et al. [43] and also with the findings from the numerical experiments carried out using the P2/P0 and P2/P1 elements during this work.

Remark: It is observed that optimal convergence rates for both the displacement ($\mathcal{O}(h^3)$) and stress ($\mathcal{O}(h^2)$) fields are obtained using the BT2/BT0 element when the pressure field is constant throughout the domain.

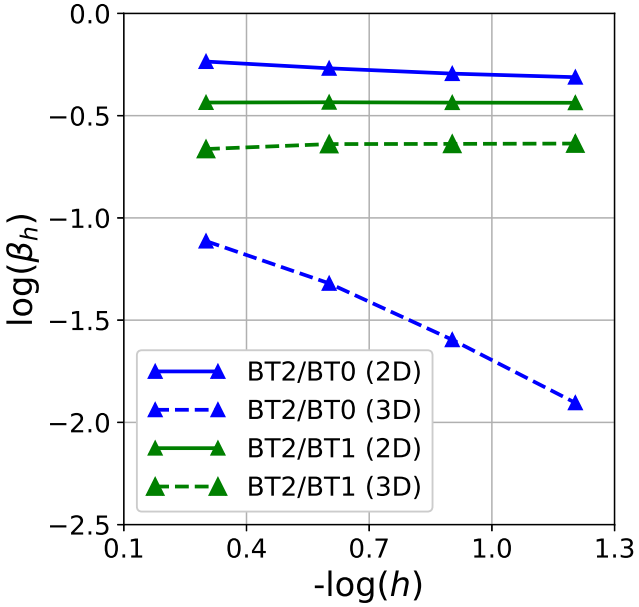

Figure 1: Example with the manufacturing solution: numerical inf-sup constant with respect to mesh refinement for BT2/BT0 and BT2/BT1 elements. The domain is of unit size in each direction and Dirichlet boundary conditions are applied on all the boundary nodes.

From the above observations, it is evident that BT2/BT1 element is superior to BT2/BT0 element both in terms of accuracy and stability. The only disadvantage of BT2/BT1 element is its increased computational effort because of the increased size of the global matrix system. However, since the number linear tetrahedron is usually about fives times the number of nodes in a given mesh, the number of additional nodal DOFs for the pressure field for BT2/BT1 element is about five times lower than that of BT2/BT0 element. The overall increase in the size of the global matrix system for the BT2/BT1 element can be shown to be about 4-5% when compared with the BT2 element, i.e., quadratic tetrahedron element with pure displacement formulation. The increased computational effort for this slight increase in the size of the global system is worth the cost, especially considering the superior accuracy of the computed numerical solutions.

On the other hand, even though BT2/BT0 might appear to be a poor element because of its substandard convergence and stability properties, it has a unique advantage over BT2/BT1 that the global matrix system can be condensed into an effective system of equations consisting only of displacement degrees of freedom, thus, enabling its implementation into the existing finite element codes based on pure displacement DOFs. Moreover, despite its instability and poor convergence rate, BT2/BT0 element does indeed produce reasonably accurate results as demonstrated with the numerical examples in Sections. 3 and 4.

Thus, with varying degrees of accuracy, stability and computational cost, the elements, BT2/BT1 and BT2/BT0 offer flexibility in choosing a displacement-pressure combination depending upon one's requirements on the accuracy and computational efficiency. Furthermore, both the combinations can be used for the development of explicit schemes without the need for transforming the governing equations into the rate-form. Thus, the elements BT2/BT1 and BT2/BT0 facilitate the development of a unified mixed formulation that can perform elastostatic, implicit elastodynamic as well as explicit elastodynamic simulations.

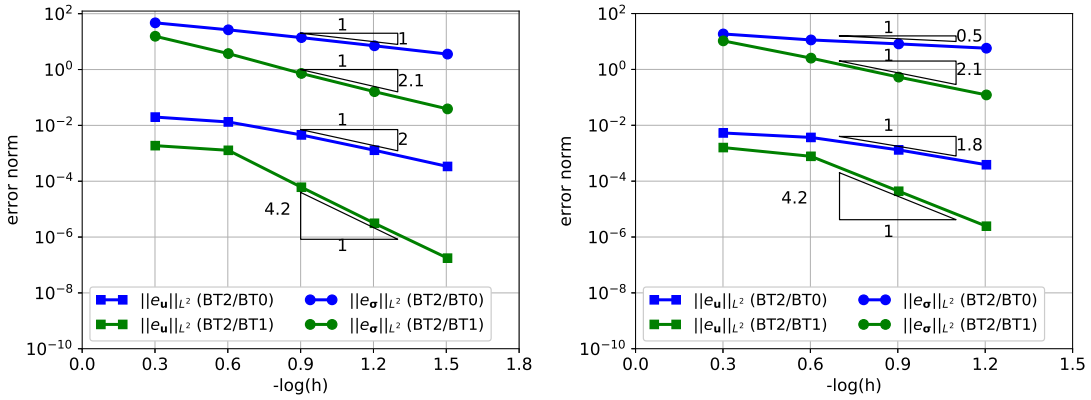

(a) Error norms for the 2D problem

(b) Error norms for the 3D problem

Figure 2: Example with the manufacturing solution: the domain is of unit size in each direction. The material parameters are: $E = 100$ and $\nu = 0.499$. The analytical solution for the 2D problem is: $u_x = 0.001\,\sin(\pi x)\,\cos(\pi y)$, $u_y = 0.001\,\cos(\pi x)\,\sin(\pi y)$ and for the 3D problem is: $u_x = 0.001\,\sin(\pi x)\,\cos(\pi y)\,\sin(\pi z)$, $u_y = 0.001\,\cos(\pi x)\,\sin(\pi y)\,\sin(\pi z)$, $u_z = 0.001\,\cos(\pi x)\,\cos(\pi y)\,\cos(\pi z)$. Body force is computing from the analytical solution and the Dirichlet boundary conditions are applied on all the boundary nodes.

2.3.2 Implicit time integration

By adapting the scheme of [38] to obtain the implicit solutions of Eq. (48) and using the Newton-Raphson scheme to solve the resulting nonlinear equations, we get the following discrete matrix system for the incremental displacements, $\Delta\mathbf{u}$, and incremental pressure, $\Delta\mathbf{p}$,

$$\begin{bmatrix} \mathbf{K}_{uu}^{\text{mixed}} & \mathbf{K}_{up} \\ \mathbf{K}_{pu} & -\mathbf{K}_{pp} \end{bmatrix} \begin{Bmatrix} \Delta\mathbf{u} \\ \Delta\mathbf{p} \end{Bmatrix} = - \begin{Bmatrix} \mathbf{R}_u^{\text{mixed}} \\ \mathbf{R}_p \end{Bmatrix} \tag{51}$$

where

$$\mathbf{K}_{uu}^{\text{mixed}} = \frac{\alpha_m^2}{\alpha_f \gamma^2 \Delta t^2}\,\mathbf{M}_{uu} + \alpha_f \widehat{\mathbf{K}}_{\text{M}} + \alpha_f \widehat{\mathbf{K}}_{\text{G}} \tag{52}$$

$$\mathbf{K}_{up} = \alpha_f \int_\omega \mathbf{B}^{\text{T}}\,\mathbf{m}\mathbf{N}_p\;\text{d}\omega \tag{53}$$

$$\mathbf{K}_{pu} = \alpha_f \int_\omega \frac{1}{\kappa}\,\frac{\partial^2 U}{\partial J^2}\bigg|_{\boldsymbol{u}^k_{n+\alpha_f}} \mathbf{N}_p^{\text{T}}\,\text{m}^{\text{T}}\mathbf{B}\;\text{d}\omega \tag{54}$$

$$\mathbf{K}_{pp} = \alpha_f \int_\Omega \frac{1}{\kappa}\,\mathbf{N}_p^{\text{T}}\mathbf{N}_p\;\text{d}\Omega \tag{55}$$

$$\mathbf{R}_u^{\text{mixed}} = \mathbf{M}_{uu}\,\mathbf{a}^k_{n+\alpha_m} + \mathbf{F}^{\text{int,mixed}}(\mathbf{u}^k_{n+\alpha_f}, \mathbf{p}^k_{n+\alpha_f}) - \mathbf{F}^{\text{ext}}_{n+\alpha_f}. \tag{56}$$

The matrices, $\widehat{\mathbf{K}}_{\text{M}}$ and $\widehat{\mathbf{K}}_{\text{G}}$, are computed using

$$\widehat{\mathbf{K}}_{\text{M}} = \int_\omega \mathbf{B}^{\text{T}}\,\widehat{\mathbf{D}}\,\mathbf{B}\;\text{d}\omega, \quad \text{and} \quad \widehat{\mathbf{K}}_{\text{G}} = \int_\omega \mathbf{G}^{\text{T}}\,\widehat{\boldsymbol{\Sigma}}\,\mathbf{G}\;\text{d}\omega. \tag{57}$$

where $\widehat{\Sigma}_{ijkl} = \widehat{\sigma}_{jl}\delta_{ik}$, and the material tangent matrix, $\widehat{\mathbf{D}}$, is computed using

$$\widehat{\mathbf{D}} = \mathbf{I}_{\text{dev}}\mathbf{D}\mathbf{I}_{\text{dev}} \;-\; \frac{2}{3}\left(\mathbf{m}\overline{\boldsymbol{\sigma}}^{\text{T}}_{\text{dev}} + \overline{\boldsymbol{\sigma}}_{\text{dev}}\mathbf{m}^{\text{T}}\right) \;+\; 2\,(\bar{p} - p)\,\mathbf{I}_0 \;-\; \left(\frac{2}{3}\bar{p} - p\right)\mathbf{m}\mathbf{m}^{\text{T}}. \tag{58}$$

Matrix condensation for BT2/BT0 element: For computationally efficient solution of coupled matrix system (51) when using BT2/BT0 element, it can be rewritten as

$$\left[\mathbf{K}_{uu}^{\text{mixed}} + \mathbf{K}_{up}\,\mathbf{K}_{pp}^{-1}\,\mathbf{K}_{pu}\right]\,\Delta\mathbf{u} = -\mathbf{R}_u - \mathbf{K}_{up}\,\mathbf{K}_{pp}^{-1}\,\mathbf{R}_p \tag{59}$$

$$\mathbf{K}_{pp}\,\Delta\mathbf{p} = \mathbf{K}_{pu}\,\Delta\mathbf{u} + \mathbf{R}_p \tag{60}$$

By exploiting the constant-discontinuous approximation used for the pressure field, i.e., $\mathbf{N}_p = 1$, for the BT2/BT0 element, the additional stiffness term, $\mathbf{K}_{up}\,\mathbf{K}_{pp}^{-1}\,\mathbf{K}_{pu}$, and the additional force term, $\mathbf{K}_{up}\,\mathbf{K}_{pp}^{-1}\,\mathbf{R}_p$, can be evaluated element-wise before assembling into the global matrix and vector. Now, the condensed equation (59) can be solved first for the incremental displacements, $\Delta\mathbf{u}$, and then the incremental pressure, $\Delta\mathbf{p}$, can be evaluated element-wise as

$$\Delta p^e = \frac{\kappa}{\alpha_f\, V_0^e}\,\left[\mathbf{K}_{pu}^e\,\Delta\mathbf{u}^e + R_p^e\right]. \tag{61}$$

The crucial steps involved in the mixed formulation with the implicit scheme using BT2/BT1 element are presented as pseudocode in Algorithm 1. The pseudocode for the implicit scheme using BT2/BT0 element is analogous to the Algorithm 1 but with minor modifications in the assembly and solution phases.

Algorithm 1 Algorithm for the mixed formulation with implicit scheme

Set: Parameters α_m, α_f, γ and tolerance, ϵ
Initialise: $\mathbf{u}_0$, $\mathbf{v}_0$, $\mathbf{p}_0$, $\dot{\mathbf{u}}_0$ and $\mathbf{a}_0 = \mathbf{M}_{uu}^{-1}(\mathbf{F}_0^{\text{ext}} - \mathbf{F}_0^{\text{int}})$
for $t \leq t_{\text{final}}$ **do**
    Compute: $\mathbf{F}_{n+\alpha_f}^{\text{ext}}$
    Predict: $\mathbf{u}_{n+1}^{(1)} = \mathbf{u}_n$, $\mathbf{p}_{n+1}^{(1)} = \mathbf{p}_n$
    for k=1 to *max-iter* **do**
        Compute: $\mathbf{v}_{n+1}^{(k)}$, $\mathbf{a}_{n+1}^{(k)}$, $\mathbf{u}_{n+\alpha_f}^{(k)}$, $\mathbf{v}_{n+\alpha_f}^{(k)}$, $\mathbf{a}_{n+\alpha_m}^{(k)}$ and $\mathbf{p}_{n+\alpha_f}^{(k)}$
        Compute: $\mathbf{K}_{uu}^{\text{mixed},e}$, $\mathbf{K}_{up}^e$, $\mathbf{K}_{pu}^e$, $\mathbf{K}_{pp}^e$, $\mathbf{R}_u^e$, R_p^e
        Assemble: RHS and LHS in (51)
        if $|-\{\mathbf{R}_u^{\text{mixed}} \quad \mathbf{R}_p\}^{\text{T}}| \leq \epsilon$ **then**
            Converged, exit iteration loop
        end if
        Solve: For $\Delta\mathbf{u}$ and $\Delta\mathbf{p}$ in (51)
        Update: $\mathbf{u}_{n+1}^{(k+1)} = \mathbf{u}_{n+1}^{(k)} + \Delta\mathbf{u}$; $\quad \mathbf{p}_{n+1}^{(k+1)} = \mathbf{p}_{n+1}^{(k)} + \Delta\mathbf{p}$
    end for
    Compute: $\dot{\mathbf{u}}_{n+1}$ from (24)
    Update: $(\mathbf{u}_n, \mathbf{v}_n, \mathbf{a}_n, \dot{\mathbf{u}}_n, \mathbf{p}_n) \leftarrow (\mathbf{u}_{n+1}, \mathbf{v}_{n+1}, \mathbf{a}_{n+1}, \dot{\mathbf{u}}_{n+1}, \mathbf{p}_{n+1})$
end for

2.3.3 Explicit time integration

The fully discrete system of equations for the explicit scheme for the mixed formulation (48) can be written as

$$\mathbf{M}_{uu}\,\mathbf{a}_{n+1} = \mathbf{F}_n^{\text{ext}} - \mathbf{F}_n^{\text{int,mixed}} \tag{62a}$$

$$\mathbf{u}_{n+1} = \mathbf{u}_n + \Delta t\,\mathbf{v}_n + \Delta t^2\,\left[\left(\frac{1}{2} - \beta\right)\,\mathbf{a}_n + \beta\,\mathbf{a}_{n+1}\right] \tag{62b}$$

$$\mathbf{v}_{n+1} = \mathbf{v}_n + \Delta t\,\left[(1-\gamma)\,\mathbf{a}_n + \gamma\,\mathbf{a}_{n+1}\right] \tag{62c}$$

$$\mathbf{M}_{pp}\,\mathbf{p}_{n+1} = \int_\Omega \mathbf{N}_p^{\text{T}}\,\frac{\partial U}{\partial J}\bigg|_{\mathbf{u}_{n+1}}\,\mathrm{d}\Omega. \tag{62d}$$

Here, $\mathbf{F}_n^{\text{int,mixed}}$ is the internal force vector given by Eq. (49) and evaluated using the known solution $(\mathbf{u}_n, \mathbf{p}_n)$ at time instant t_n, and $\mathbf{M}_{pp}$ is the mass matrix for the pressure field and it is given as

$$\mathbf{M}_{pp} = \int_\Omega \mathbf{N}_p^{\text{T}}\,\mathbf{N}_p\;\mathrm{d}\Omega. \tag{63}$$

Now, similar to the explicit scheme for the displacement formulation, equation (62a) is solved for the accelerations, $\mathbf{a}_{n+1}$, using the lumped matrix approximation of $\mathbf{M}_{uu}$, followed by updates to the displacements and velocities using equations (62b) and (62c), respectively. Finally, pressure degrees of freedom are updated by solving (62d). The solution of pressure field using equation (62d) poses no computational difficulties for BT2/BT0 element due to the fact that the matrix $\mathbf{M}_{pp}$ for BT2/BT0 element is already diagonal

with each diagonal entry being the volume of the element in the original configuration. For the computationally efficient solution of pressure field when using BT2/BT1 element, equation (62d) is solved using lumped mass matrix approximation for $\mathbf{M}_{pp}$. The pseudocode for the explicit scheme for the mixed formulation is presented in Algorithm. 2.

At this point, it is important to point out the significance of equation (62d) which can be interpreted as a least-squares solution of the relation between hydrostatic pressure and the volumetric energy function given in (45). The success of the proposed explicit scheme stems from the fact that the pressure DOFs in equation (62d) can be evaluated element-wise for BT2/BT0 element, and using a lumped mass matrix for BT2/BT1 element, once the displacement DOFs are computed using equation (62b). Thus, both the combinations BT2/BT1 and BT2/BT0 help to develop a unified finite element framework that can perform elastostatic, implicit elastodynamic as well as explicit elastodynamic simulations using a single finite element formulation that does not require any sophisticated modifications and/or additional stabilisations.

Algorithm 2 Algorithm for the mixed formulation with explicit scheme

Set: Parameters γ, β and CFL
Compute: $\mathbf{M}_{uu}$ and $\mathbf{M}_{pp}$ as lumped mass matrices
Initialise: $\mathbf{u}_0$, $\mathbf{v}_0$, $\mathbf{v}_0$ and $\mathbf{a}_0 = \mathbf{M}_{uu}^{-1}(\mathbf{F}_0^{\text{ext}} - \mathbf{F}_0^{\text{int,mixed}})$
for $t \leq t_{\text{final}}$ **do**
    Compute: $\mathbf{F}_n^{\text{ext}}$ and $\mathbf{F}_n^{\text{int,mixed}}$
    Compute: characteristic length, h
    Compute: $\Delta t = \frac{\text{CFL}\, h}{c}$
    Solve: $\mathbf{M}_{uu}\, \mathbf{a}_{n+1} = \mathbf{F}_n^{\text{ext}} - \mathbf{F}_n^{\text{int,mixed}}$
    Compute: $\mathbf{u}_{n+1} = \mathbf{u}_n + \Delta t\, \mathbf{v}_n + \Delta t^2 \left[\left(\frac{1}{2} - \beta\right) \mathbf{a}_n + \beta\, \mathbf{a}_{n+1}\right]$
    Compute: $\mathbf{v}_{n+1} = \mathbf{v}_n + \Delta t \left[(1-\gamma)\, \mathbf{a}_n + \gamma\, \mathbf{a}_{n+1}\right]$
    Solve: $\mathbf{M}_{pp}\, \mathbf{p}_{n+1} = \int_\Omega \mathbf{N}_p^{\text{T}} \left.\frac{\partial U}{\partial J}\right|_{\mathbf{u}_{n+1}} \text{d}\Omega$
    Update: $(\mathbf{u}_n, \mathbf{v}_n, \mathbf{a}_n, \mathbf{p}_n) \leftarrow (\mathbf{u}_{n+1}, \mathbf{v}_{n+1}, \mathbf{a}_{n+1}, \mathbf{p}_{n+1})$
end for

3 Numerical examples - static problems

Before presenting the examples on elastodynamics, the spatial convergence of the proposed scheme is established by studying some well-known elastostatic benchmark examples in this section. All the meshes used in the present work are obtained by applying a mapping technique over the corresponding quadratic Lagrange elements generated using HyperMesh [44]. We refer the reader to [31] for the discussion on the mapping techniques for the mesh generation and application of Dirichlet boundary conditions for the quadratic Bézier elements.

The stiffness matrix and internal force vectors are evaluated using 3-point Gauss quadrature rule for triangular elements and 4-point rule for tetrahedral elements, and the consistent mass matrix is evaluated using 7-point quadrature rule for the triangular elements and 11-point quadrature rule for the tetrahedron element. All the applied external traction loads are assumed to be *dead loads*, meaning that the force vectors due to the applied tractions are evaluated in the original configuration of the domain.

It has been observed that, for elastostatic and implicit elastodynamic simulations, numerical results obtained with the P2/P0 and P2/P1 elements are identical to those obtained, respectively, with the BT2/BT0 and BT2/BT1 elements. Therefore, for the sake of clarity and, more importantly, since higher-order Lagrange elements are not amenable for explicit schemes, numerical results obtained using Lagrange elements are not included in this paper. Nevertheless, numerical results obtained in this work are compared with those obtained with *subdivision-stabilised mixed formulation using quadratic NURBS* proposed in Kadapa et al. [34]; thus, providing the relative performance of the proposed elements in the context of isogeometric analysis. For convenience in the discussion of results, various elements considered in this work are denoted using the following abbreviations:

Material models:

- For the examples with purely elastic material, the material model is assumed to be a nearly incompressible Neo-Hookean material model with the strain energy density given by the following function,

BT2	—	Element with pure displacement formulation with quadratic Bézier triangle for 2D problems and quadratic Bézier tetrahedron for 3D problems.
BT2/BT0	—	Element with mixed formulation with quadratic Bézier triangle/tetrahedron for displacement and element-wise constant value for pressure.
BT2/BT1	—	Element with mixed formulation with quadratic Bézier triangle/tetrahedron for displacement and linear Bézier triangle/tetrahedron for pressure.
Q_2/Q_2-SD	—	Element with subdivision-stabilised mixed formulation with quadratic NURBS.

unless otherwise stated.

$$W(J,\bar{\mathbf{C}}) = \frac{1}{2}\mu\left(\mathrm{I}_{\bar{\mathbf{C}}} - 3\right) + \frac{1}{2}\kappa\left(\frac{1}{2}(J^2-1) - \ln J\right) \tag{64}$$

where $\kappa = E/3(1-2\nu)$ is the Bulk modulus and $\mu = E/2(1+\nu)$ is the shear modulus, with E as the Young's modulus and ν as the Poisson's ratio.

- For the examples with elastoplastic materials, the material model is assumed to the hyperelastic extension of the J_2-flow theory with an uncoupled stored energy function which consists of Neo-Hookean model (64) for the elastic deformations and a plasticity model with associative flow rule based on the von Mises yield criterion with isotropic nonlinear hardening/softening for given by

$$k(\alpha) = \sigma_y + (\sigma_\infty - \sigma_y)\left[1 - \exp(-\delta\alpha)\right] + H\alpha, \text{with} \quad \delta > 0 \tag{65}$$

for the plastic portion. Here, α is the equivalent plastic strain, σ_y is the initial yield stress, σ_∞ is the saturation yield stress, δ is the saturation exponent and H is the linear hardening/softening coefficient. For the in-depth discussion on the theoretical aspects and computer implementation of elastoplastic models in finite strains, we refer the reader to the works of Simo and Hughes [45] and de Souza Neto et al. [36].

3.1 Cook's membrane in two dimensions

In this example, the bending behaviour of the proposed elements is assessed using the example of Cook's membrane modelled with the Neo-Hookean hyperelastic and von Mises elastoplastic material models. The geometry and boundary conditions of the problem and a set of successively refined meshes are shown in Figure 3.

For the Neo-Hookean model, Young's modulus and Poisson's ratio are assumed to be $E = 240.565$ MPa and $\nu = 0.4999$, respectively, and the applied traction force is, $F = 100$ N/mm. The plot of vertical displacement of point A against the number of elements per side shown in Figure 4a illustrates the apparent convergence of the proposed elements and proves that the results obtained with the present work match well with the reference solution. The contour plots of pressure presented in Figure 5 show that the pressure field obtained with both the mixed elements is free from spurious oscillations.

For the von Mises elastoplastic material model, the material properties are: bulk modulus, $\kappa = 164.21$ GPa; shear modulus, $\mu = 80.1938$ GPa; initial yield stress, $\sigma_y = 0.450$ GPa; saturation yield stress, $\sigma_\infty = 0.715$ GPa; saturation exponent, $\delta = 16.93$; and linear hardening coefficient, $H = 0.12924$ GPa. The analysis is performed for a load value of $F = 20$ kN/mm. The vertical displacement of point A shown in Figure 4b demonstrates the clear convergence of the proposed formulation towards the reference solution. While the difference between the contour plots of equivalent plastic strain obtained with all the three elements is negligible, as shown in Figure 6, the pressure field obtained with both the mixed elements is free from spurious oscillations, as presented in Figure 7.

The convergence graphs in Figure 4 illustrate that the solution obtained with BT2/BT0 element converges from above while that of BT2/BT1 convergences from below, and the results obtained with the coarse meshes indicate that BT2/BT0 element is softer and BT2/BT1 element is stiffer when compared with the Q_2/Q_2-SD element. Most importantly, these graphs demonstrate that accurate numerical results can be obtained with the proposed elements using very coarse meshes. The quality of results obtained using BT2/BT0 element is also quite remarkable, considering especially that the spatial convergence rates for this element are one order lower than those of BT2/BT1 element. It is this ability of the proposed work to compute accurate numerical results using very coarse meshes that makes it very computationally appealing.

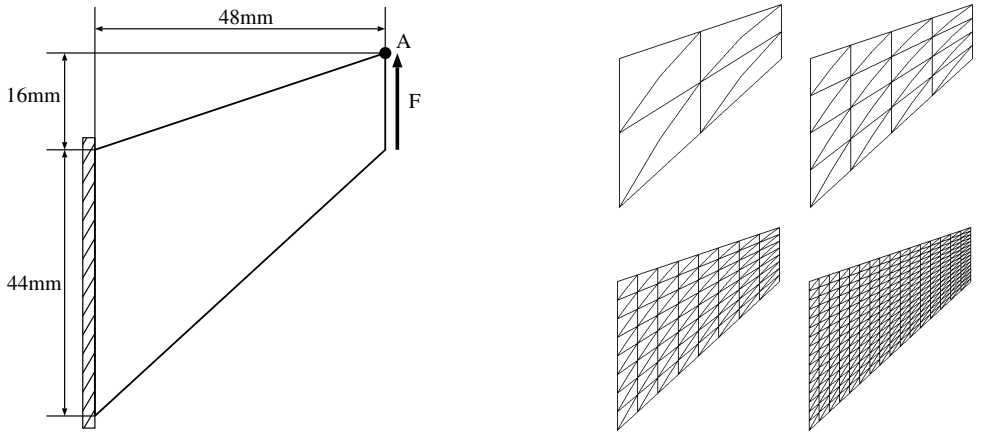

(a) (b)

Figure 3: Cook's membrane: (a) geometry and boundary conditions and (b) first four meshes used for the analysis.

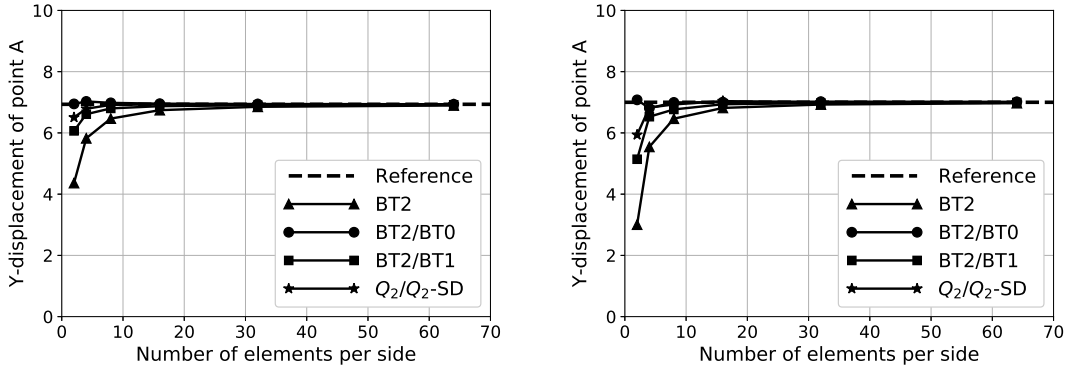

(a) Neo-Hookean material (b) Elastoplastic material

Figure 4: Cook's membrane: convergence of vertical displacement of point A with (a) Neo-Hookean hyperelastic material model and (b) elastoplastic material model. The reference solution is from [34].

3.2 Compression of a plane-strain block

This problem is proposed by Reese et al. [46], and it serves as an excellent benchmark example to assess the performance of numerical formulations for two-dimensional problems undergoing large compressive deformations. The geometry and boundary conditions of the problem are as shown in Figure 8. Due to the symmetry of geometry, boundary conditions and the applied pressure load, only a half portion of the model is considered for the analysis. The analysis is performed for the maximum loading condition of p/p_0=60 with $p_0 = 20$, over a set of structured and unstructured meshes shown, respectively, in Figures 9 and 10, in order to assess the accuracy and robustness of the proposed elements over arbitrarily oriented meshes under severe compressive deformations.

The accuracy of the numerical results is assessed by studying the vertical displacement of point A as the mesh is refined. Plots of percentage compression presented in Figure 11 illustrate that present results are in good agreement with the reference solution. These graphs also indicate that the results obtained with the pure displacement formulation also match well with the reference solution. Contour plots of the pressure field presented in Figures 12 and 13 illustrate that the pressure field obtained with the mixed formulation is completely free from spurious oscillations, and the pressure field obtained with the displacement formulation is also not wholly unacceptable. However, *the displacement formulation has been found to be computationally very expensive*; the displacement formulation requires 120 load steps for the successful completion of the simulation while the mixed formulation with BT2/BT0 or BT2/BT1 element requires only six load steps.

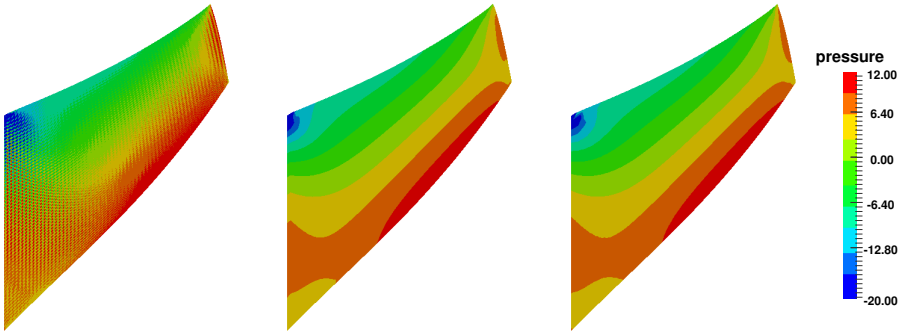

(a) BT2 (b) BT2/BT0 (c) BT2/BT1

Figure 5: Cook's membrane: contour plots of pressure with Neo-Hookean material with $(32 \times 32) \times 2$ mesh.

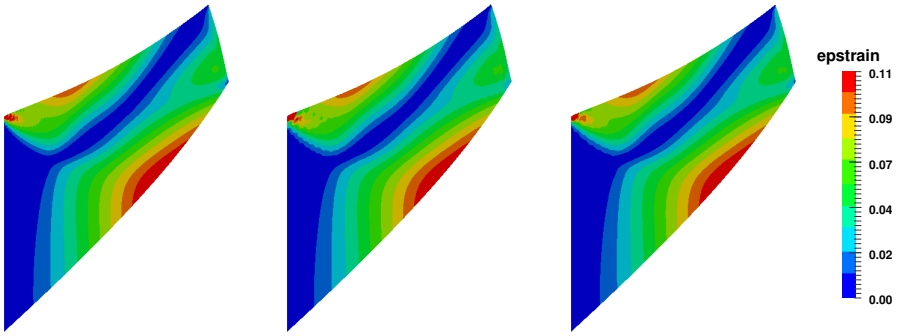

(a) BT2 (b) BT2/BT0 (c) BT2/BT1

Figure 6: Cook's membrane: contour plots of equivalent plastic strain with $(32 \times 32) \times 2$ mesh.

3.3 Compression of a block in 3D

This benchmark problem, proposed by Reese et al. [47], is a 3D extension of the previous example. Due to the symmetry and boundary conditions, only a quarter portion of the model, as shown in Figure 14a, is considered for the analysis. For this problem, a nearly incompressible Neo-Hookean material model whose strain energy density function is given as

$$W(J, \bar{\mathbf{C}}) = \frac{1}{2}\mu\,(\mathrm{I}_{\bar{\mathbf{C}}} - 3) + \frac{\lambda}{2}(\ln J)^2 \tag{66}$$

with $\lambda = 400888.2$ MPa and $\mu = 80.19$ MPa, is considered. Simulations are performed over five finite element meshes shown in Figure 15 using both the displacement and mixed formulations for a maximum load value of $p/p_0 = 80$ with $p_0 = 4$ N/mm^2.

The accuracy of numerical results is assessed using Z-displacement of point A, as shown in Figure 14a, in terms of the percentage of compression against the number of elements per side. This graph shows that the difference between the results obtained with the proposed mixed elements and the Q_2/Q_2-SD element is negligible for all the discretisations except for the first mesh in the sequence. This graphs also illustrates that both the formulations produce accurate displacement solutions even for the very coarse meshes. However, it is important to point out that, even though the displacement solutions obtained with BT2 elements are not entirely far off from the reference solution, the disadvantage of BT2 elements is that they not only produce erratic stress fields, as shown in Figures 16 and 17, but also are computationally more expensive since they require a substantially higher number of load steps for the successful completion of the simulation. On the contrary, in addition to producing smooth fields, BT2/BT0 and BT2/BT1 elements require fewer load steps. For this example, BT2 elements require 40 load steps whereas both the mixed elements require only five load steps. It is also important to highlight the accuracy of the results obtained with the BT2/BT0 element in spite of its instability with respect to the inf-sup condition and poor spatial convergence rate for the linear problem.

Thus, with *the ability to obtain accurate numerical results with fewer load steps using very coarse structured/unstructured tetrahedral element meshes that can be readily generated using the existing mesh generators*, the proposed work offers significant benefits in performing the simulations of complex, large-

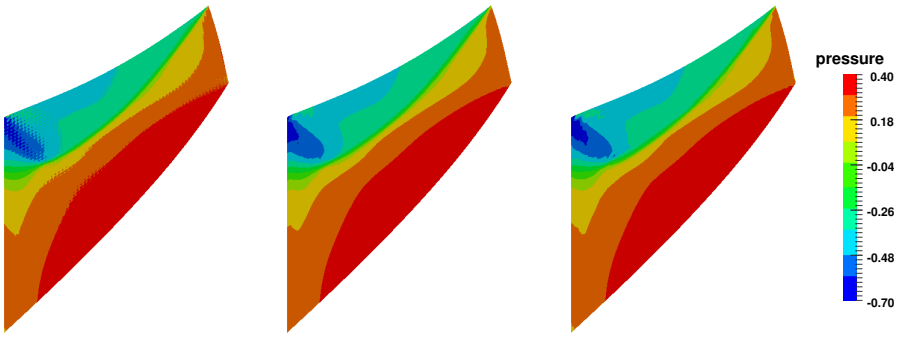

(a) BT2 (b) BT2/BT0 (c) BT2/BT1

Figure 7: Cook's membrane: contour plots of pressure with elastoplastic material with $(32 \times 32) \times 2$ mesh.

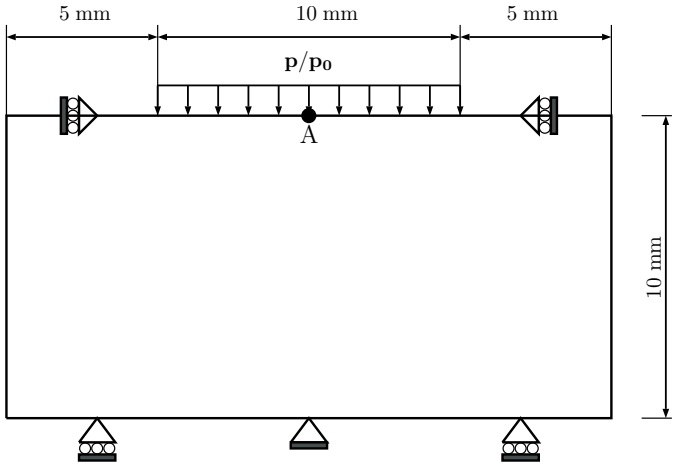

Figure 8: Plane-strain block: geometry and boundary conditions.

scale problems encountered in the industry.

3.4 Thin semi-cylindrical shell with a point load

This example is concerned with the study of one of the popular shell benchmarks. The problem consists of a thin semi-cylindrical shell that is fixed at one end and pinched with a radially inward point load at its free end. The geometry and boundary conditions of the problem are depicted schematically in Figure 18, together with two of the meshes used for the analysis. The dimensions of the shell are: length, $L = 3.048$; radius of the center circle, $R = 1.016$; and thickness, $h = 0.03$. The material properties are: modulus of elasticity, $E = 2.0685 \times 10^7$ and Poisson's ratio, $\nu = 0.3$. The magnitude of the point load is, $P = 2000$. Due to the symmetry of geometry and loading conditions, only a half portion of the domain is considered for the analysis.

The evolution of radial displacement of point A with respect to the load factor is plotted in Figure 19. These load-deflection curves obtained with the proposed elements match very well with the reference solution. Figure 20 shows the final deformed configurations of the shell overlaid with the contour plots of element-wise stresses. The results obtained for this example demonstrate the ability of the present work in successfully overcoming the issue of *shear locking* frequently encountered with the lower-order elements in modelling shell structures. Thus, this example illustrate the applicability of the present work to a wide range of challenging problems in solid mechanics.

4 Numerical examples - dynamic problems

For the implicit scheme, the spectral radius is chosen as $\rho_\infty = 0$ so that all the high-frequency modes are damped, and the time step is chosen to be uniform and sufficiently small enough. For the explicit scheme,

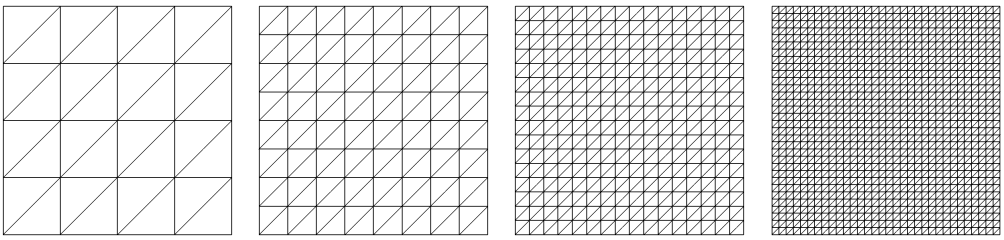

(a) Mesh M1-stru (b) Mesh M2-stru (c) Mesh M3-stru (d) Mesh M4-stru

Figure 9: Plane-strain block: structured meshes.

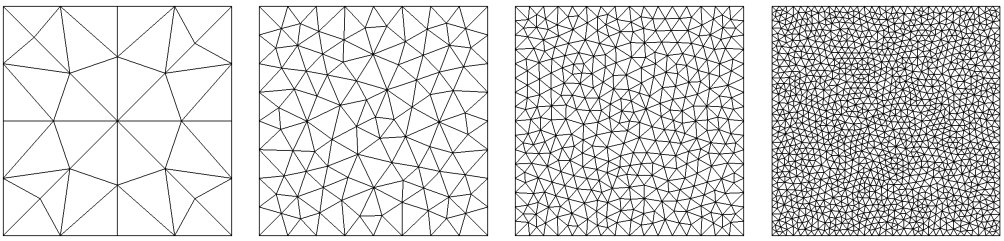

(a) Mesh M1-unstru (b) Mesh M2-unstru (c) Mesh M3-unstru (d) Mesh M4-unstru

Figure 10: Plane-strain block: unstructured meshes.

the time step is computed as

$$\Delta t = \frac{\text{CFL}\, h}{c} \quad \text{with} \quad c = \sqrt{\frac{\kappa + 4\,\mu/3}{\rho}}, \tag{67}$$

where c is the bulk wave speed, CFL is the Courant-Friedrichs-Lewy number, and h is the characteristic length which is taken as the half of the minimum edge length. CFL number is taken as 0.75 in all the example presented in this work. The characteristic length is evaluated at the configuration corresponding to the previous time instant. The main motivation behind using the adaptive time step is that it improves the computational efficiency for the problems which experience significant deformations.

4.1 2D beam excited with initial velocity

In this example, we study the dynamic behaviour of a 2D beam problem studied in [28]. The beam is of size 1m $\times$ 6m, and it is clamped at its bottom edge and excited with a uniform initial velocity of 10 m/s in the X direction. The Young's modulus of the material is $E = 17$ MPa, and its density is $\rho = 1100$ kg/m^3. The material model for this example is Neo-Hookean hyperelastic. The numerical experiments carried out for this example reveal that the BT2 elements are sufficient enough to obtain accurate numerical results for the values of Poisson's ratio up to 0.48, which is in accordance with the convergence studies presented in [31]; therefore, we consider $\nu = 0.499$ in this example to demonstrate the true benefits of the mixed formulation. We consider three uniform and structured meshes, M1, M2 and M3, which consists of 2, 4 and 8 elements, respectively, across the thickness of the beam.

The evolution of X-displacement of the midpoint of the free end of the beam, referred to as point A henceforth, shows clear convergence with respect to mesh refinement for both the displacement and mixed formulations as shown in Figure 21; the superior convergence of BT2/BT1 elements is attributed to their optimal spatial convergence rates. The graphs presented in Figure 22 illustrate that solutions obtained with the explicit scheme match well with the corresponding values obtained with the implicit scheme. Contour plots shown in Figures 23 and 24 demonstrate that the pressure field obtained with the mixed elements (BT2/BT0 and BT2/BT1) is free from spurious oscillations, while the pressure field obtained with the BT2 elements is not completely unacceptable.

4.2 Twisting of a column

In this example, we assess the performance of the proposed finite element scheme under extremely large deformations by studying the problem of twisting of a column studied in [29]. The geometry of the problem

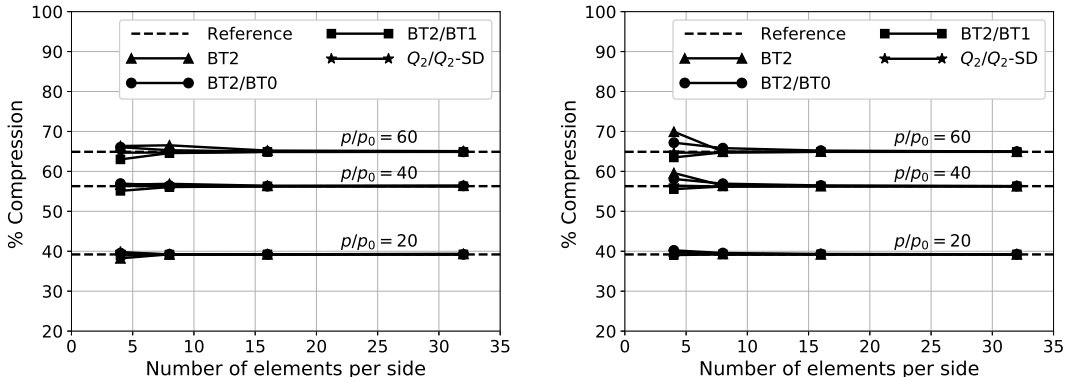

(a) structured meshes (b) unstructured meshes

Figure 11: Plane-strain block: percentage of compression of point A. The reference solution is taken from [34].

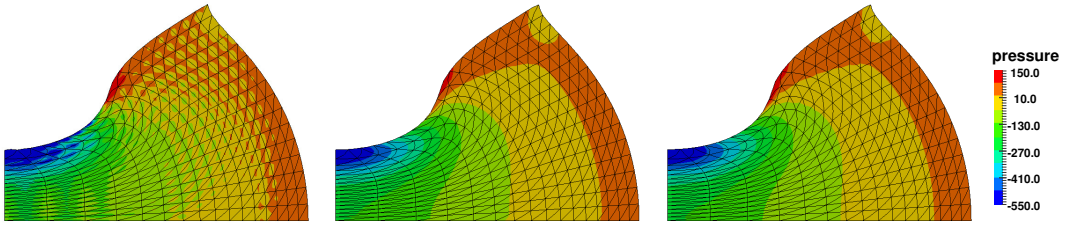

(a) BT2 (b) BT2/BT0 (c) BT2/BT1

Figure 12: Plane-strain block: contours of pressure obtained with the M3-stru mesh for $p/p_0 = 60$.

and the finite element meshes used for the analysis are shown in Figure 25. The column is clamped at its bottom face and excited with an initial velocity, $\boldsymbol{v} = (z, 0, -x)\, 100.0\, \sin(\pi\, y/12)$. The material model for this example is assumed as Neo-Hookean hyperelastic with Young's modulus, $E = 17$ MPa; Poisson's ratio, $\nu = 0.499$; and density, $\rho = 1100$ kg/m^3.

It has been observed from the numerical results that the difference between the short-term displacement response obtained with BT2, BT2/BT0 and BT2/BT1 elements is negligible for all the meshes considered and that the difference in the long-term response vanishes as the mesh is refined, as shown in Figure 26 using the solutions obtained with M1 and M2 meshes and the implicit scheme.

The evolution of Y-displacement of point A shown in Figure 27 for the M1 mesh indicates that the solutions obtained with the implicit and explicit schemes follow the same trend; the difference between the explicit solution and implicit solution is due to the use of lumped mass matrix in the explicit scheme and consistent mass matrix in the implicit scheme, as can be verified with the implicit solution obtained the lumped mass matrices. Figure 28 illustrates the convergence of the proposed method as the mesh is refined, which can also be substantiated with the comparison of deformed shapes presented in Figures 29 and 30. Contour plots in Figures 31 and 32 show that the pressure field obtained with both the mixed elements is completely free from spurious oscillations. From these plots, it can also be observed that the pressure field obtained with the proposed scheme is in excellent agreement with the reference solution. From these results, it is also worth pointing out that the quality of results obtained with the BT2/BT0 element is quite remarkable in spite of its instability and poor convergence rate.

4.3 Taylor impact test

In this example, we apply the proposed scheme to study another well-known benchmark, the Taylor impact test. The test consists of an impact a cylindrical bar of length 0.0324 m and diameter 0.0032 m against a rigid frictionless wall. The speed of impact of the bar is 227 m/s. Due to the symmetry of geometry, boundary and loading conditions, only a quarter portion of the domain is considered for the analysis. Simulations are performed using the two finite element meshes shown in Figure 33. The symmetry boundary condition is enforced on the flat faces parallel to the axis of the bar, and roller boundary condition is enforced on the

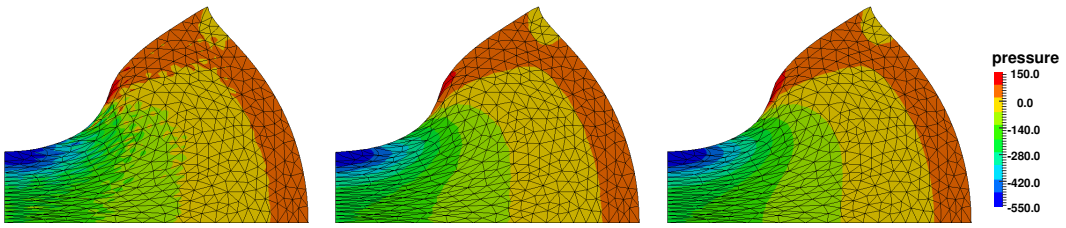

(a) BT2 (b) BT2/BT0 (c) BT2/BT1

Figure 13: Plane-strain block: contours of pressure obtained with the M3-unstru mesh for $p/p_0 = 60$.

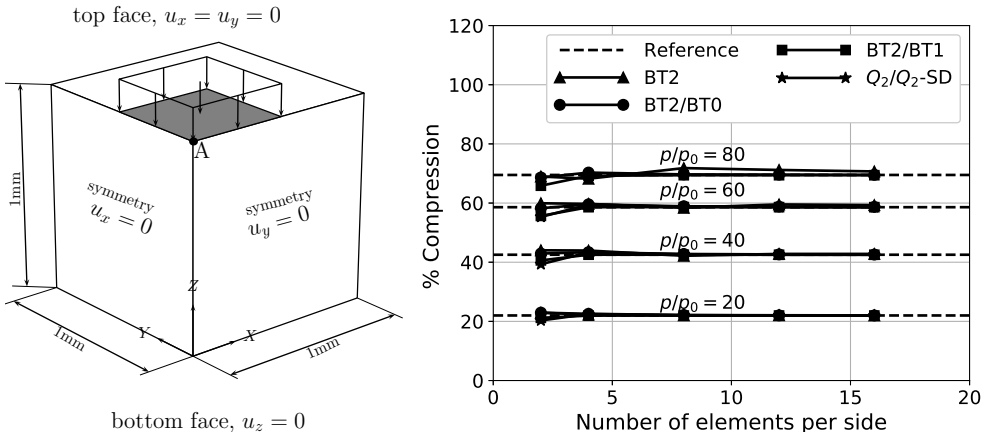

(a) (b)

Figure 14: Block compression in 3D: (a) geometry and boundary conditions and (b) compression level of point A. Reference solution is obtained with the higher-order NURBS based isogeometric analysis of [33].

circular flat face located at the leftmost end of the bar shown in Figure 33. The material model is elastoplastic with modulus of elasticity, $E = 117$ GPa; Poisson's ratio, $\nu = 0.35$; yield stress, $\sigma_y = \sigma_\infty = 0.4$ GPa; hardening modulus, $H = 0.1$ GPa; and density, $\rho_0 = 8930$ kg/m^3.

Following the published literature for this example, simulations are performed for the duration of 80 microseconds for both the meshes using all the three proposed elements and the evolution of radius of the bar at the contact surface is plotted in Figure 34. These graphs show that the present results match very well with the reference solution. The results obtained with the coarse mesh M1 with all the formulations are also not completely far off from the reference solution. As shown in Figure 35, the final deformed shapes obtained with mesh M2 using implicit and explicit schemes with BT2, BT2/BT0 and BT2/BT1 elements have a negligible difference with respect to each other. Contour plots of equivalent plastic strain presented in Figure 36 show that there is not a pronounced difference in the values of equivalent plastic strain obtained with different formulations. Contour of the pressure field shown in Figure 37 indicate that the only drawback of the BT2 element is the localised oscillatory pressure field in the vicinity of the highly deformed elements and that the mixed elements certainly help in getting rid of these oscillations in the pressure field.

These results demonstrate the ability of the proposed work to perform accurate implicit as well as explicit simulations of very challenging nonlinear elastodynamic problems using such coarse meshes as used for this very challenging example showcases the true potential of the present work in making a genuinely significant impact in performing the simulations of complex industrial problems. The fact that the explicit time integration scheme used in this work is only of single-step, besides being third-order accurate, unlike the explicit Runge-Kutta methods which require multi-step evaluations for higher-order accuracy, makes the proposed work even more computationally appealing.

4.4 Impulsively loaded elastoplastic cylindrical panel

This example, taken from [49], consists of a 120^o cylindrical panel loaded impulsively with an initial inward radial velocity of 5650 in/sec. The geometry and boundary conditions of the problem and the finite element

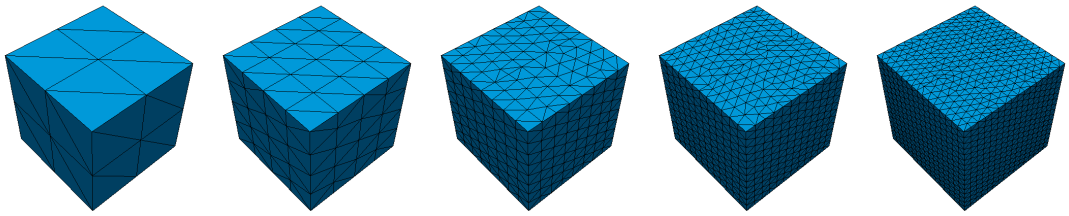

(a) Mesh M1 (b) Mesh M2 (c) Mesh M3 (d) Mesh M4 (e) Mesh M5

Figure 15: Block compression in 3D: meshes used for the analysis. The meshes M1, M2, M3, M4 and M5 have 2, 4, 8, 12 and 16 elements along each edge of the cube.

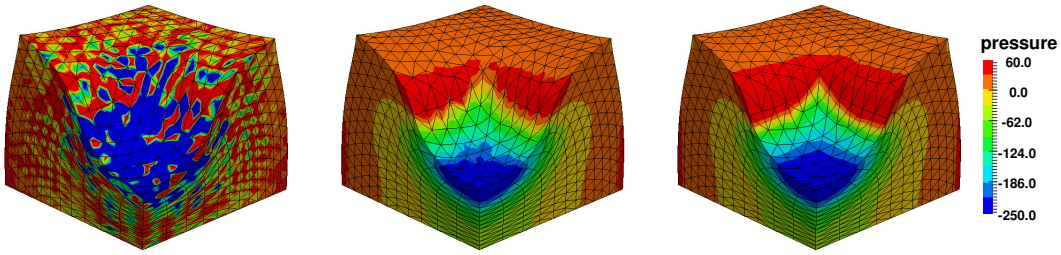

(a) BT2 (b) BT2/BT0 (c) BT2/BT1

Figure 16: Block compression in 3D: nodal contour plots of pressure with mesh M4.

mesh used for the analysis are as shown in Figure 38. Only half a portion of the domain is considered for the analysis due to the symmetry of geometry and loading conditions. The material is assumed to be elastic-perfectly-plastic with Young's modulus, $E = 1.05 \times 10^7$ psi; Poisson's ratio, $\nu = 0.33$; yield stress, $\sigma_y = 4.4 \times 10^4$ psi; and density, $\rho = 2.5 \times 10^{-4}$ lb-s^2/in^4. Simulations are performed only with the explicit schemes.

The evolution of the radial displacement of the centre point of the panel is plotted in Figure 39 along with the reference values from published literature, shows that the results obtained with the proposed scheme are in good agreement with the reference solutions. Contour plots of equivalent plastic strain and pressure presented in Figure 40 illustrate that the difference between the equivalent plastic strain obtained with the displacement and mixed elements is not significant and that the mixed formulation certainly filters out the spurious oscillations in the pressure field; these observations are in analogous with those made in the Taylor impact test example. Results presented for this example showcase, once again, the capability of the proposed scheme in performing accurate explicit simulations of a wider variety of challenging problems in nonlinear elastodynamics.

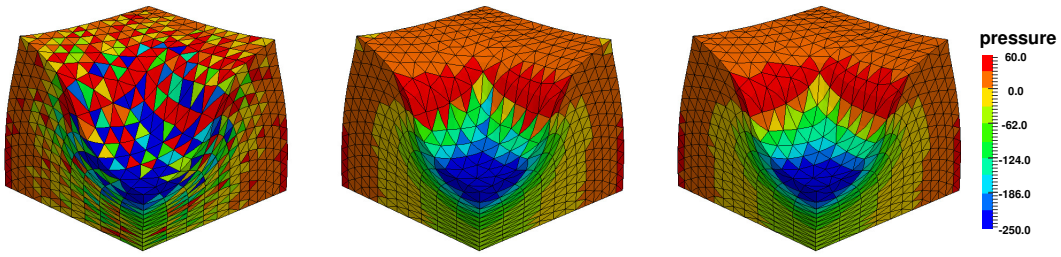

(a) BT2 (b) BT2/BT0 (c) BT2/BT1

Figure 17: Block compression in 3D: element-wise contour plots of pressure with mesh M4.

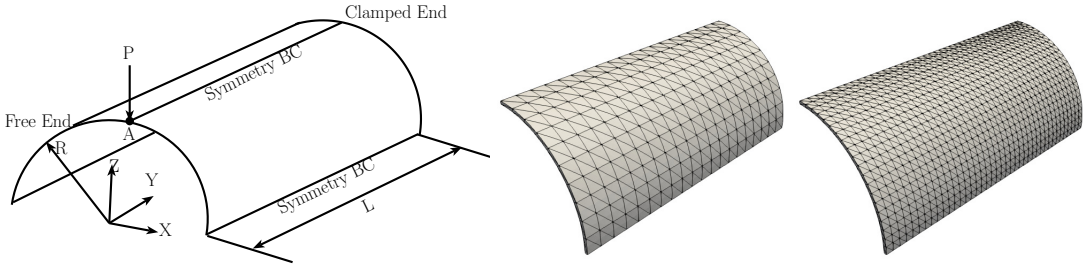

(a) geometry and boundary conditions (b) Mesh M1 (c) Mesh M2

Figure 18: Thin shell: schematic description of the problems and finite element meshes used. Meshes M1 and M2 consist of $(10 \times 20 \times 1) \times 6$ and $(20 \times 40 \times 2) \times 6$ elements.

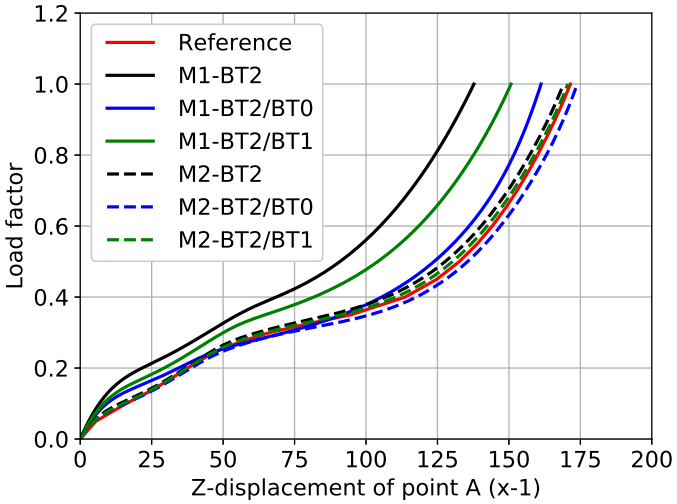

Figure 19: Thin shell: load-deflection curve with different meshes. The reference solution is from [48].

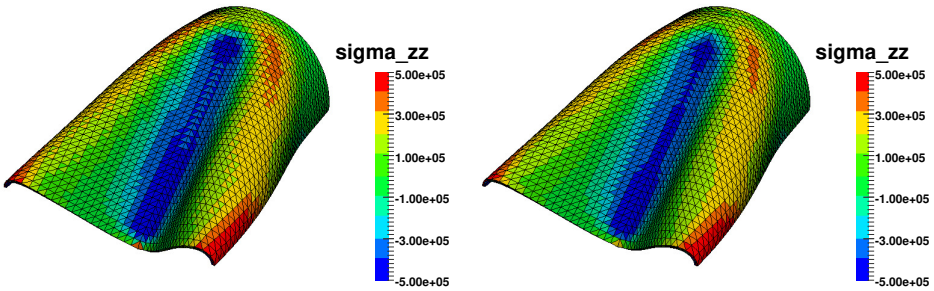

(a) BT2/BT0 (b) BT2/BT1

Figure 20: Thin shell: element-wise contour plots of σ_{zz} stress obtained with M2 mesh.

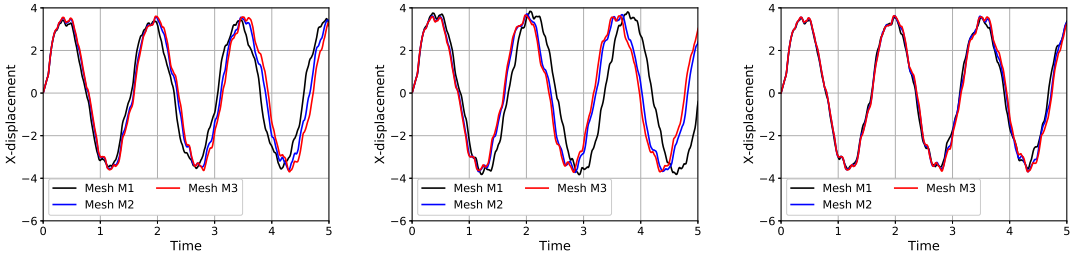

(a) BT2 (b) BT2/BT0 (c) BT2/BT1

Figure 21: 2D beam: evolution of X-displacement of point A obtained with the explicit scheme.

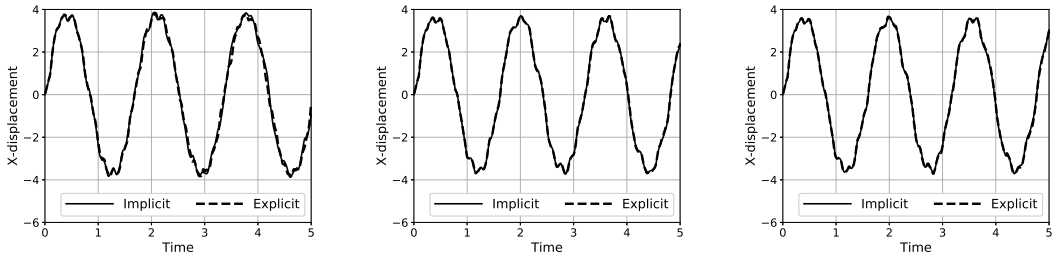

(a) Mesh M1 (b) Mesh M2 (c) Mesh M3

Figure 22: 2D beam: evolution of X-displacement of point A using BT2/BT0 elements.

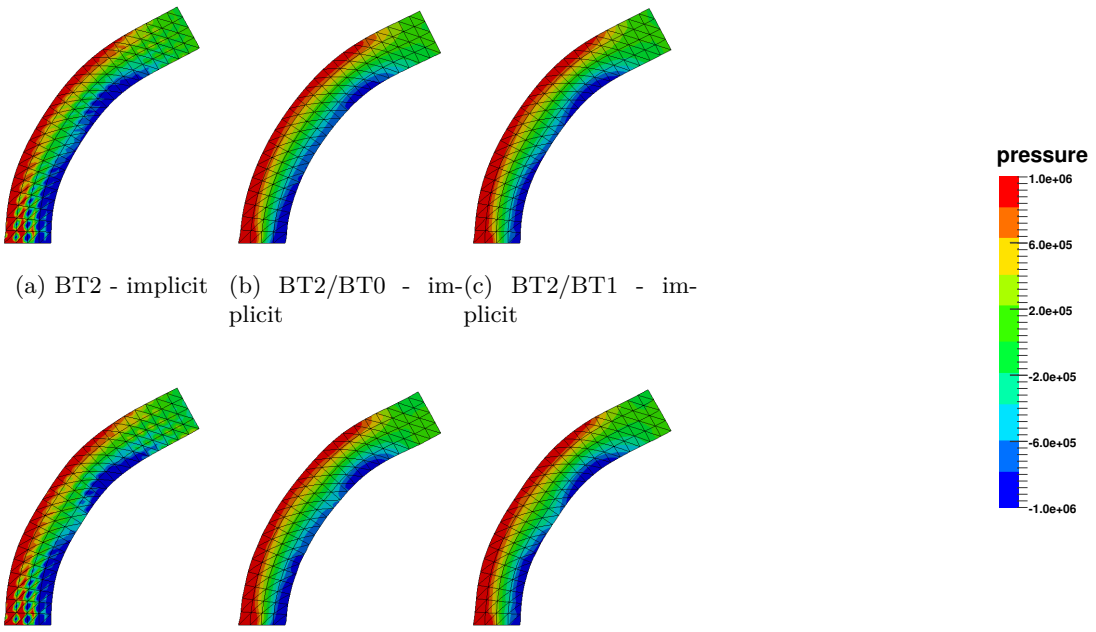

(a) BT2 - implicit (b) BT2/BT0 - implicit (c) BT2/BT1 - implicit

(d) BT2 - explicit (e) BT2/BT0 - explicit (f) BT2/BT1 - explicit

Figure 23: 2D beam: contour plots of pressure at $t = 0.5$ obtained with the mesh M2.

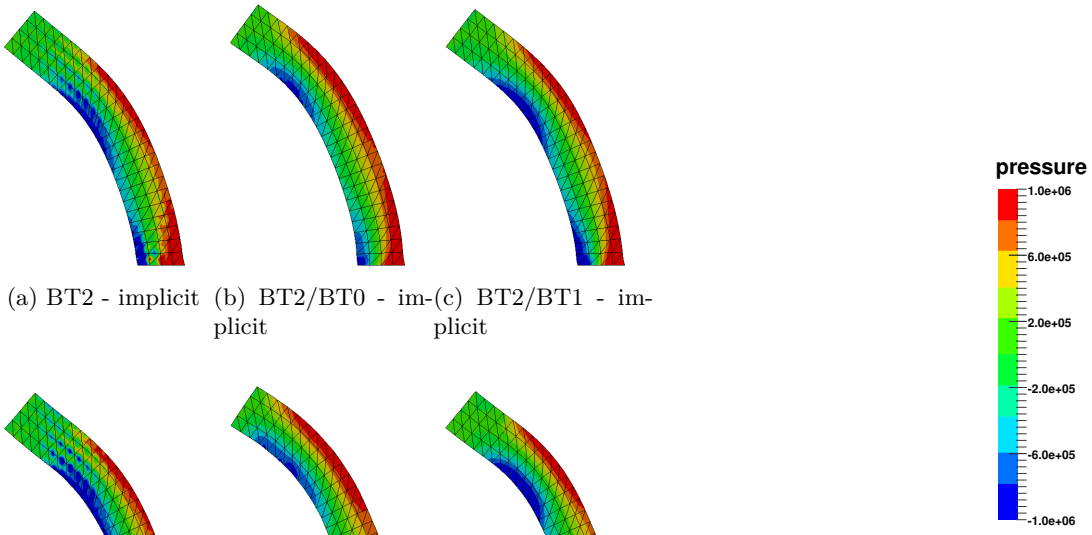

(a) BT2 - implicit (b) BT2/BT0 - implicit (c) BT2/BT1 - implicit

(d) BT2 - explicit (e) BT2/BT0 - explicit (f) BT2/BT1 - explicit

Figure 24: 2D beam: contour plots of pressure at $t = 1.0$ obtained with the mesh M2.

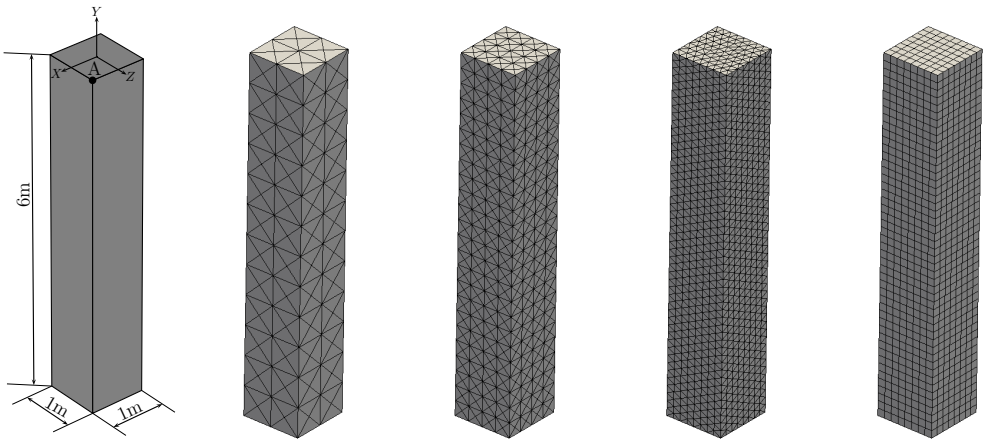

(a) Geometry (b) Mesh M1 (c) Mesh M2 (d) Mesh M3 (e) Mesh M4

Figure 25: Twisting column: geometry and meshes used for the analysis. Mesh M4 is used to obtain the solution with Q_2/Q_2-SD elements.

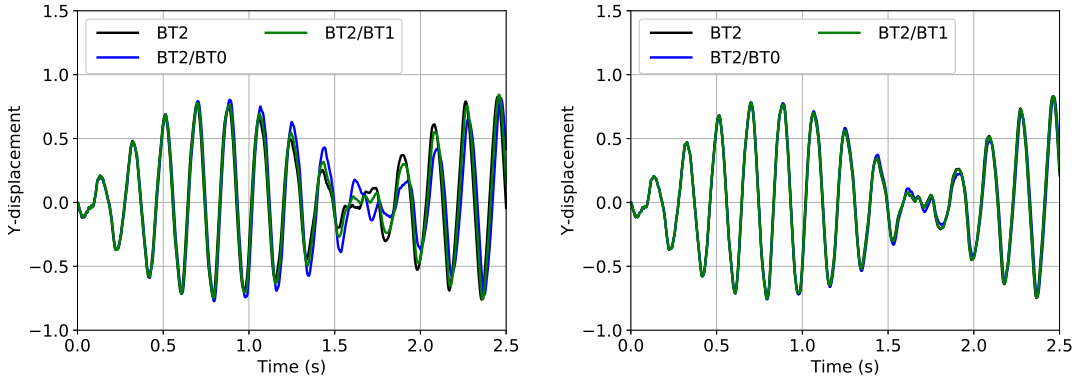

(a) M1 mesh (b) M2 mesh

Figure 26: Twisting column: evolution of Y-displacement of point A using the implicit scheme.

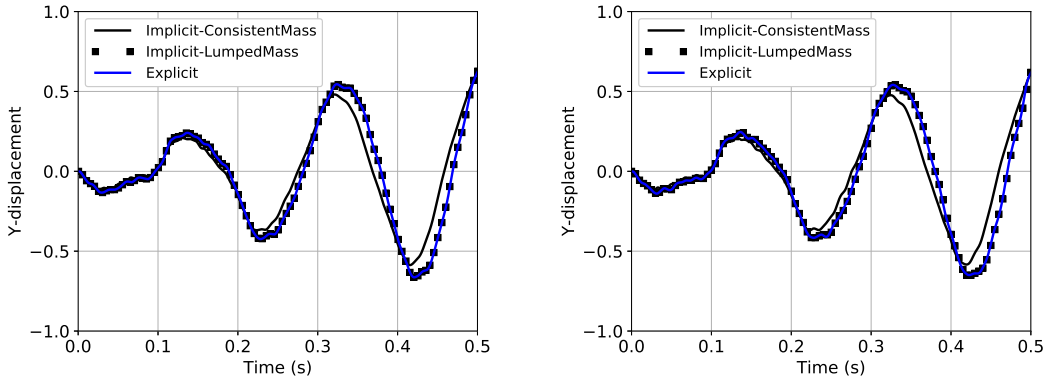

(a) BT2 (b) BT2/BT1

Figure 27: Twisting column: evolution of Y-displacement of point A with mesh M1.

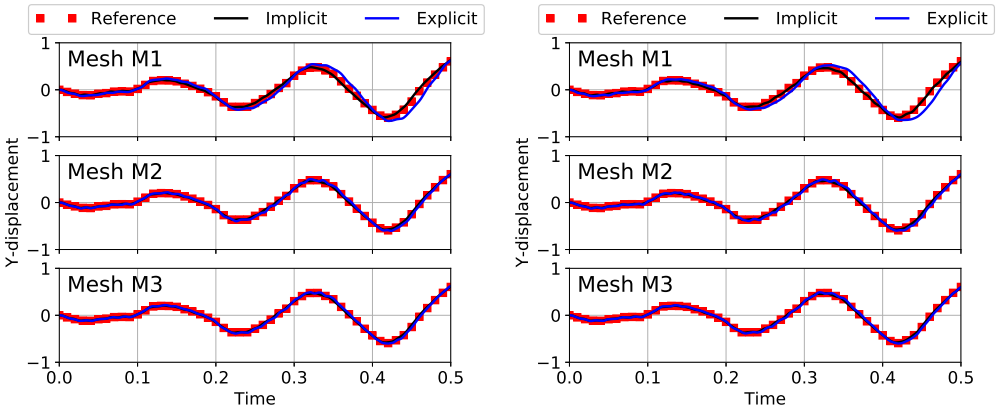

(a) BT2 (b) BT2/BT1

Figure 28: Twisting column: evolution of Y-displacement of point A with different meshes using implicit and explicit formulations. The reference solution is obtained with mesh M4 using Q_2/Q_2-SD elements and the implicit scheme.

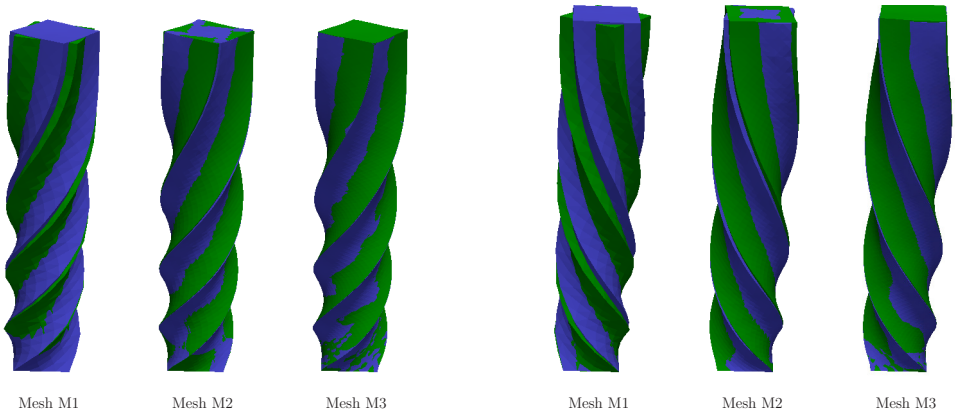

(a) $t = 0.1$ (b) $t = 0.3$

Figure 29: Twisting column: deformed shapes at (a) $t = 0.1$ and (b) $t = 0.3$, obtained with M1, M2 and M3 meshes using implicit (green) and explicit (purple) schemes with BT2/BT0 elements.

(a) $t = 0.1$, implicit(b) $t = 0.3$, implicit(c) $t = 0.1$, explicit(d) $t = 0.3$, explicit

Figure 30: Twisting column: deformed shapes obtained with the implicit and explicit schemes with BT2/BT1 elements with the meshes M1 (green), M2 (blue), M3 (red) and M4 (gray).

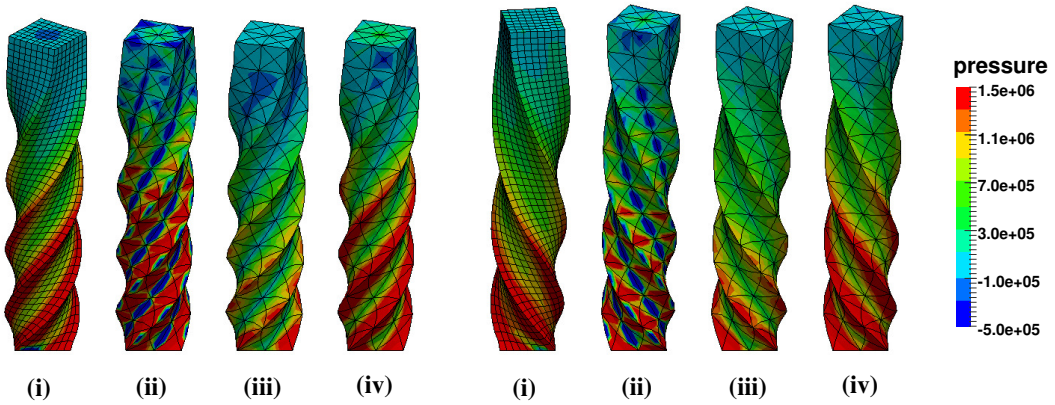

(a) $t = 0.1$ (b) $t = 0.3$

Figure 31: Twisting column: contour plots of pressure at $t = 0.1$ and $t = 0.3$. In each subfigure, (i) mesh M4 with Q_2/Q_2-SD elements and implicit scheme, (ii) mesh M1 with BT2 elements and explicit scheme, (iii) mesh M1 with BT2/BT0 elements and explicit scheme and (iv) mesh M1 with BT2/BT1 elements and explicit scheme.

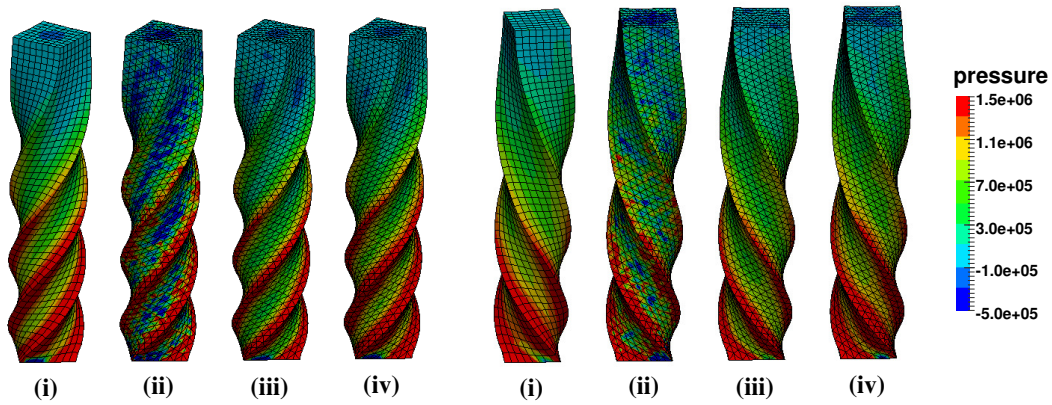

(a) $t = 0.1$ (b) $t = 0.3$

Figure 32: Twisting column: contour plots of pressure at $t = 0.1$ and $t = 0.3$. In each subfigure, (i) mesh M4 with Q_2/Q_2-SD elements and implicit scheme, (ii) mesh M3 with BT2 elements and explicit scheme, (iii) mesh M3 with BT2/BT0 elements and explicit scheme and (iv) mesh M3 with BT2/BT1 elements and explicit scheme.

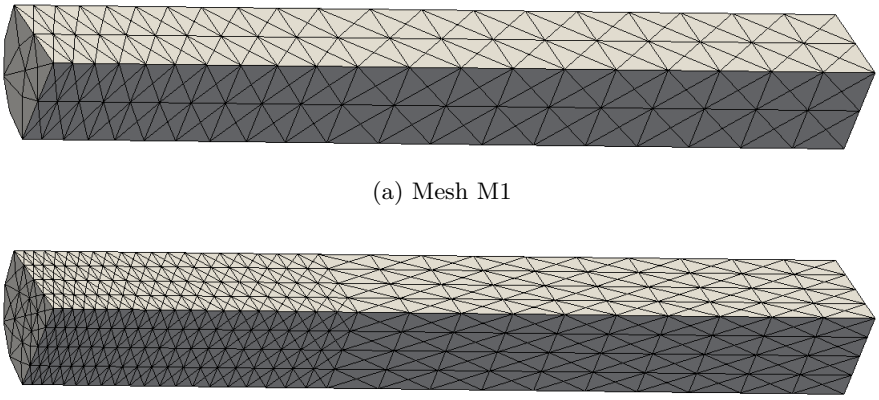

(a) Mesh M1

(b) Mesh M2

Figure 33: Taylor impact test: meshes used for the finite element analysis.

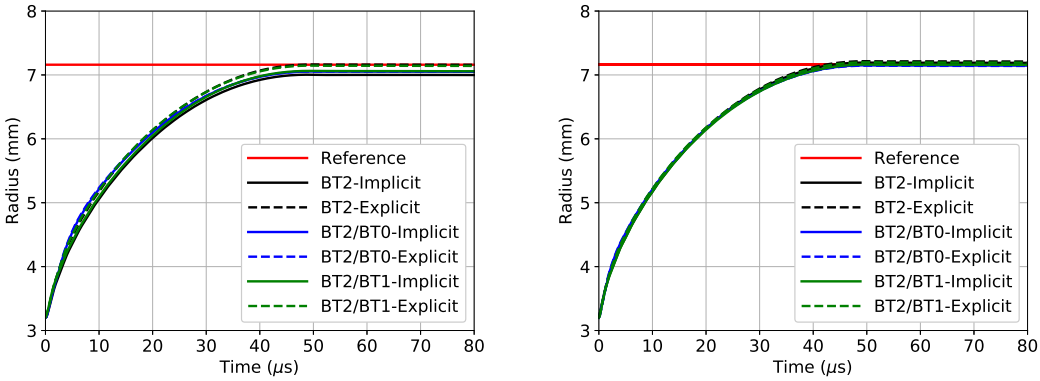

(a) Mesh M1 (b) Mesh M2

Figure 34: Taylor impact test: evolution of radius of the bar at the impact face. The reference solution is from Zienkiewicz et al. [1].

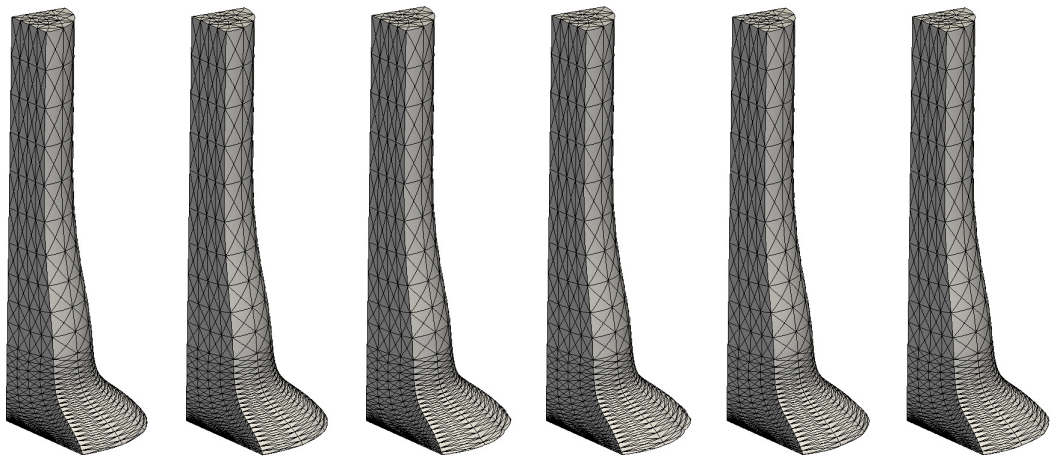

(a) (b) (c) (d) (e) (f)

Figure 35: Taylor impact test: deformed shapes at $t = 80\mu$s obtained with mesh M2: (a) BT2 - implicit, (b) BT2 - explicit, (c) BT2/BT0 - implicit, (d) BT2/BT0 - explicit, (e) BT2/BT1 - implicit and (f) BT2/BT1 - explicit

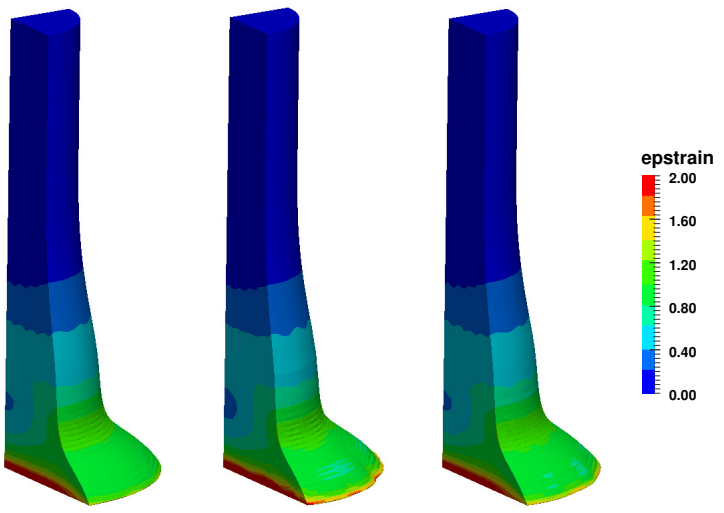

(a) BT2 (b) BT2/BT0 (c) BT2/BT1

Figure 36: Taylor impact test: contour plots of equivalent plastic strain at $t = 80\mu$s obtained with mesh M2 using the explicit scheme.

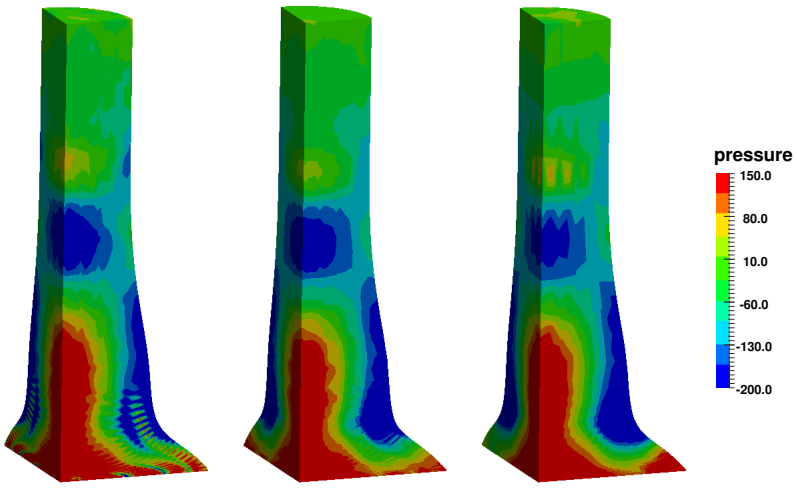

(a) BT2 (b) BT2/BT0 (c) BT2/BT1

Figure 37: Taylor impact test: contour plots of pressure at $t = 80\mu$s obtained with mesh M2 using the explicit scheme.

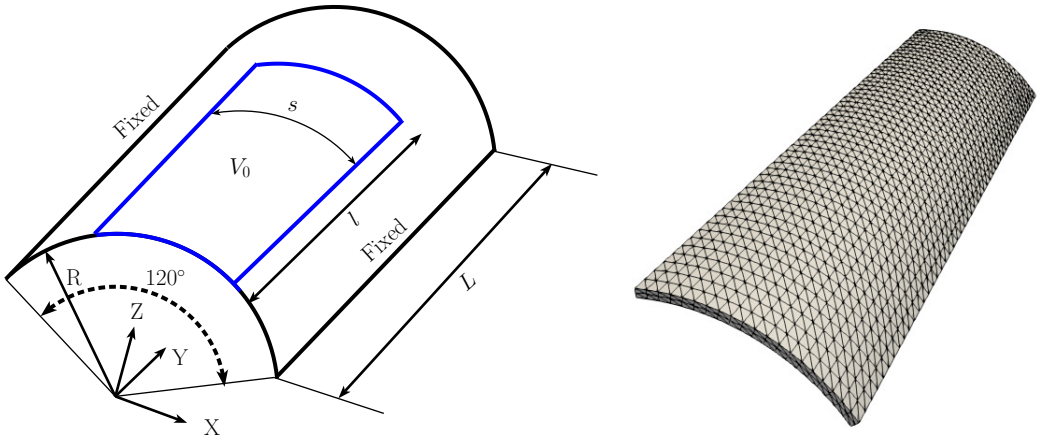

(a) (b)

Figure 38: Impulsively loaded cylindrical panel: (a) geometry and boundary conditions and (b) finite element mesh used for the analysis. The initial velocity is applied only to the portion of the domain that is bounded by the blue lines.

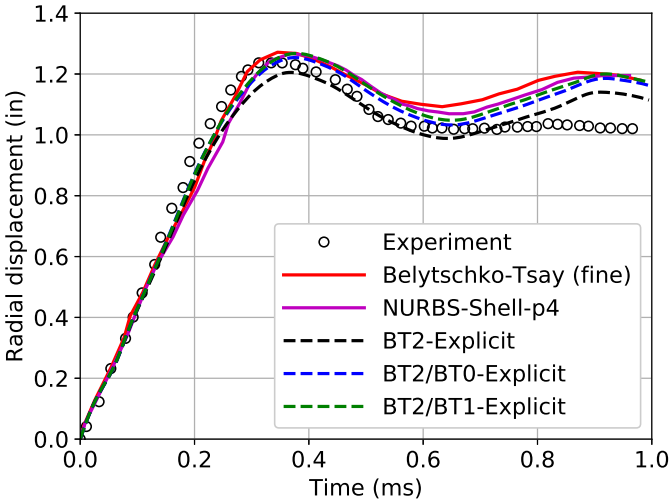

Figure 39: Impulsively loaded cylindrical panel: evolution of radial displacement. The reference solutions for the Belytschko-Tsay shell and NURBS shell models are taken from [50].

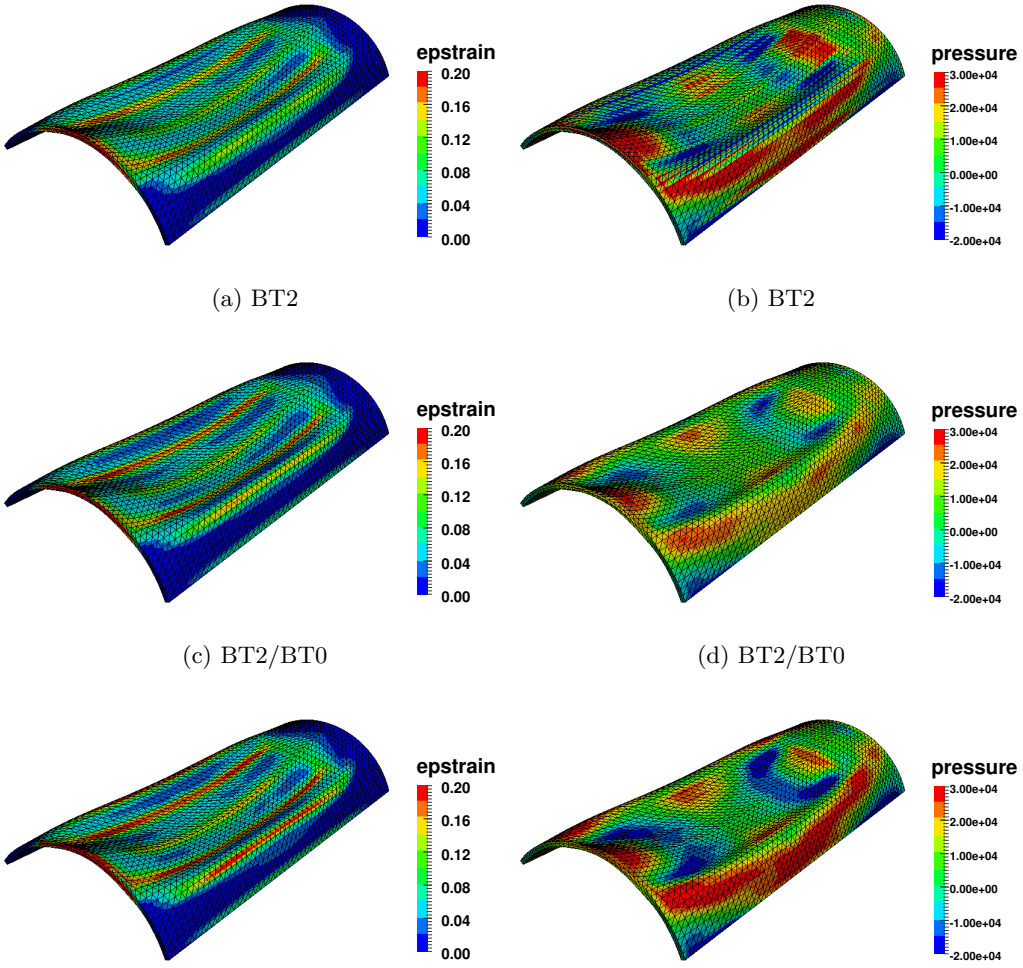

(a) BT2 (b) BT2

(c) BT2/BT0 (d) BT2/BT0

(e) BT2/BT1 (f) BT2/BT1

Figure 40: Impulsively loaded cylindrical panel: contour plots of equivalent plastic strain and pressure at $t = 0.4$ ms.

5 Summary and Conclusions

We have presented a simple, accurate and computationally efficient unified finite element framework for the computer simulation of finite strain problems in solid mechanics. The finite element formulation considered for dealing with volumetric and shear locking is the mixed displacement-pressure formulation. The novel contributions of the present work are the extension of the mixed displacement-pressure formulation to quadratic Bézier triangular and tetrahedral elements and the development of a unified finite element framework that allows for computationally efficient explicit simulations of nonlinear elastodynamics. The elements proposed in this work are abbreviated as BT2, BT2/BT0 and BT2/BT1 to distinguish them from the corresponding Lagrange elements, P2, P2/P0 and P2/P1.

The accuracy of the proposed scheme and its ability to produce accurate numerical results using coarse structured or unstructured triangular/tetrahedral meshes that can be readily generated using existing mesh generators, is demonstrated by studying several challenging elastostatic and elastodynamics benchmark examples in finite strains. The important features of the proposed work are:

- ***Versatility:*** The versatile nature of the proposed work is due to its ability to (a) perform either elastostatic or implicit elastodynamic or explicit elastodynamic simulations using a single finite element framework, and (b) efficiently deal with *volumetric-locking* as well as *shear-locking*.
- ***Computational efficiency:*** The computational efficiency of the proposed scheme is the combined result of (a) quadratic polynomials for the displacement field, (b) significantly fewer additional DOFs for the pressure field, (c) the ability to obtain accurate numerical results using coarse meshes, (d) the capability to complete simulations using fewer load steps in elastostatic simulations, and (e) single-step time integration schemes for elastodynamic simulations.
- ***Robustness:*** The robustness of the proposed work is due to the fact that it is completely free from any ad-hoc parameters that control the accuracy and stability.
- ***Ease of mesh generation:*** The finite element discretisations for the proposed work can be generated by applying a simple linear mapping, see [31], to the Lagrange elements that can be generated using the existing mesh generators.
- ***Implementability into existing FE codes:*** The mapping techniques proposed in [31], facilitate a relatively straightforward implementation of the proposed work into the existing finite element codes.

In conclusion, the above-listed features of the proposed work make it a very promising finite element framework for the computer simulation of a wide range of problems in solid mechanics. In particular, the present work has the potential to extend the capability of today's finite element codes to performing computationally efficient explicit simulations of challenging large-scale nonlinear elastodynamic problems involving nearly incompressible and elastoplastic material models.

As the future work, a straightforward extension of the proposed work would be to contact-impact simulations. Furthermore, the primary ingredients of the proposed finite element framework can be extended to develop computationally efficient explicit schemes for other challenging problems in solid and fluid mechanics.

Acknowledgements

The author acknowledges the support of the Supercomputing Wales project, which is part-funded by the European Regional Development Fund (ERDF) via the Welsh Government.

References

[1] Zienkiewicz O. C., Rojek J., Taylor R. L., Pastor M.. Triangles and Tetrahedra in explicit dynamic codes for solids. *International Journal for Numerical Methods in Engineering.* 1998;43:565-583.

[2] Bonet J., Burton A. J.. A simple average nodal pressure tetrahedral element for incompressible and nearly incompressible dynamic explicit applications. *Communications in Numerical Methods in Engineering.* 1998;14:437-449.

[3] Dohrmann C. R., Heinstein M. W., Jung J., Key S. W., Witkowski W. R.. Node-based uniform strain elements for three-node triangular and four-node tetrahedral meshes. *International Journal of Numerical Methods in Engineering.* 2000;47:1549-1568.

[4] Puso M. A., Solberg J.. A stabilized nodally integrated tetrahedral. *International Journal of Numerical Methods in Engineering.* 2006;67:841-867.

[5] He Z. C., Li G. Y., Zhong Z. H., et al. An edge-based smoothed tetrahedron finite element method (ES-T-FEM) for 3D static and dynamic problems. *Computational Mechanics.* 2013;52:221-236.

[6] de Souza Neto E. A., Andrade Pires F. M., Owen D. R. J.. F-bar-based linear triangles and tetrahedra for finite strain analysis of nearly incompressible solids. Part I: formulation and benchmarking. *International Journal of Numerical Methods in Engineering.* 2005;62:353-383.

[7] Danielson K. T.. Fifteen node tetrahedral elements for explicit methods in nonlinear solid dynamics. *Computer Methods in Applied Mechanics and Engineering.* 2014;272:160-180.

[8] Pakravan A., Krysl P.. Mean-strain 10-node tetrahedron with energy-sampling stabilization. *International Journal for Numerical Methods in Engineering.* 2017;109:1439-1460.

[9] Pakravan A., Krysl P.. Mean-strain 10-node tetrahedron with energy-sampling stabilization for nonlinear deformation. *International Journal for Numerical Methods in Engineering.* 2017;111:603-623.

[10] Hansbo P., Larson M.. Discontinuous Galerkin methods for incompressible and nearly incompressible elasticity by Nitsche's method. *Computer Methods in Applied Mechanics and Engineering.* 2002;191:1895-1908.

[11] Noels L., Radovitzky R.. An explicit discontinuous Galerkin method for non-linearsolid dynamics: Formulation, parallel implementation and scalability properties. *International Journal for Numerical Methods in Engineering.* 2007;74:1393-1420.

[12] Nguyen N. C., Pereira J.. Hybridizable discontinuous Galerkin methods for partial differential equations in continuum mechanics. *Journal of Computational Physics.* 2012;231:5955-5988.

[13] Franca L. P., Hughes T. J. R., Loula A. F. D., Miranda I.. A new family of stable elements for nearly incompressible elasticity based on a mixed Petrov-Galerkin finite element formulation. *Numerische Mathematik.* 1988;53:123-141.

[14] Klaas O., Maniatty A., Shephard M. S.. A stabilized mixed finite element method for finite elasticity. Formulation for linear displacement and pressure interpolation. *Computer Methods in Applied Mechanics and Engineering.* 1999;180:65-79.

[15] Maniatty A. M., Liu Y., Klaas O., Shephard M. S.. Stabilized finite element method for viscoplastic flow: formulation and a simple progressive solution strategy. *Computer Methods in Applied Mechanics and Engineering.* 2001;190:4609-4625.

[16] Maniatty A. M., Liu Y., Klaas O., Shephard M. S.. Higher order stabilized finite element method for hyperelastic finite deformation. *Computer Methods in Applied Mechanics and Engineering.* 2002;191:1491-1503.

[17] Masud A., Xia K.. A stabilized mixed finite element method for nearly incompressible elasticity. *Journal of Applied Mechanics.* 2005;72:711-720.

[18] Xia K., Masud A.. A stabilized Finite element formulation for finite deformation elastoplasticity in geomechanics. *Computers and Geotechnics.* 2009;36:396-405.

[19] Cervera M., Chiumenti M., Valverde Q., Saracibar C.. Mixed linear/linear simplicial elements for incompressible elasticity and plasticity. *Computer Methods in Applied Mechanics and Engineering.* 2003;192:5249-5263.

[20] Cervera M., Chiumenti M., Codina R.. Mixed stabilized finite element methods in nonlinear solid mechanics. Part I: formulation. *Computer Methods in Applied Mechanics and Engineering.* 2010;199:2559-2570.

[21] Cervera M., Chiumenti M., Codina R.. Mixed stabilized finite element methods in nonlinear solid mechanics. Part II: strain localization. *Computer Methods in Applied Mechanics and Engineering.* 2010;199:2571-2589.

[22] Cervera M., Chiumenti M., Benedetti L., Codina R.. Mixed stabilized finite element methods in nonlinear solid mechanics. Part III: compressible and incompressible plasticity. *Computer Methods in Applied Mechanics and Engineering.* 2015;285:752-775.

[23] Scovazzi G., Carnes B., Zeng X., Rossi S.. A simple, stable, and accurate linear tetrahedral finite element for transient, nearly, and fully incompressible solid dynamics: a dynamic variational multiscale approach. *International Journal for Numerical Methods in Engineering.* 2016;106:799-839.

[24] Rossi S., Abboud N., Scovazzi G.. Implicit finite incompressible elastodynamics with linear finite elements: A stabilized method in rate form. *Computer Methods in Applied Mechanics and Engineering.* 2016;311:208-249.

[25] Zeng X., Scovazzi G., Abboud N., Colomés O., Rossi S.. A dynamic variational multiscale method for viscoelasticity using linear tetrahedral elements. *International Journal for Numerical Methods in Engineering.* 2017;112:1951-2003.

[26] Scovazzi G., Song T., Zeng X.. A velocity/stress mixed stabilized nodal finite element for elastodynamics: Analysis and computations with strongly and weakly enforced boundary conditions. *Computer Methods in Applied Mechanics and Engineering.* 2017;325:532-576.

[27] Abboud N., Scovazzi G.. Elastoplasticity with linear tetrahedral elements: A variational multiscale method. *International Journal for Numerical Methods in Engineering.* 2018;115:913-955.

[28] Lee C. H., Gil A. J., Bonet J.. Development of a cell centred upwind finite volume algorithm for a new conservation law formulation in structural dynamics. *Computers and Structures.* 2013;118:13-38.

[29] Gil A. J., Lee C. H., Bonet J., Aguirre M.. A stabilised Petrov-Galerkin formulation for linear tetrahedral elements in compressible, nearly incompressible and truly incompressible fast dynamics. *Computer Methods in Applied Mechanics and Engineering.* 2014;276:659-690.

[30] Cottrell J. A., Bazilevs Y., Hughes T. J. R.. *Isogeometric analysis: toward integration of CAD and FEA*. Chichester, England: John Wiley & Sons; 2009.

[31] Kadapa C.. Novel quadratic Bézier triangular and tetrahedral elements using existing mesh generators: Applications to linear nearly incompressible elastostatics and implicit and explicit elastodynamics. *International Journal for Numerical Methods in Engineering.* 2019;117:543-573.

[32] Zienkiewicz O. C., Taylor R. L.. *The Finite Element Method for Solid and Structural Mechanics.* Oxford, England: Elsevier Butterworth and Heinemann; Sixth ed.2005.

[33] Kadapa C.. Mixed Galerkin and least-squares formulations for isogeometric analysis. PhD thesisCollege of Engineering, Swansea University2014.

[34] Kadapa C., Dettmer W. G., Perić D.. Subdivision based mixed methods for isogeometric analysis of linear and nonlinear nearly incompressible materials. *Computer Methods in Applied Mechanics and Engineering.* 2016;305:241-270.

[35] Bathe K. J.. *Finite Element Procedures.* New Jersey: Prentice Hall Inc.; 1996.

[36] de Souza Neto E. A., Perić D., Owen D. R. J.. *Computational Methods for Plasticity, Theory and Applications.* United Kingdom: John Wiley and Sons; 2008.

[37] Bonet J., Wood R. D.. *Nonlinear continuum mechanics for finite element analysis.* Cambridge University Press; 1997.

[38] Kadapa C., Dettmer W. G., Perić D.. On the advantages of using the first-order generalised-alpha scheme for structural dynamic problems. *Computers and Structures.* 2017;193:226-238.

[39] Chung J., Lee J. M.. A new family of explicit time integration methods for linear and non-linear structural dynamics. *International Journal for Numerical Methods in Engineering.* 1994;37:3961-3976.

[40] Hughes T. J. R.. *The Finite Element Method: Linear Static and Dynamic Finite Element Analysis.* Dover Publications; 2000.

[41] Brezzi F., Fortin M.. *Mixed and Hybrid Finite Element Methods.* Springer-Verlag; 1991.

[42] Chapelle D., Bathe K. J.. The inf-sup test. *Computers and Structures.* 1993;47:537-545.

[43] Gmeiner B., Waluga C., Wohlmuth B.. Local Mass-Corrections for Continuous Pressure Approximations of Incompressible Flow. *SIAM Journal on Numerical Analysis.* 2014;52:2931-2956.

[44] HyperMesh (https://altairhyperworks.com/product/HyperMesh) .

[45] Simo J. C., Hughes T. J. R.. *Computational Inelasticity.* Berlin, Germany: Springer; 1998.

[46] Reese S., Kussner M., Reddy B. D.. A new stabilization technique for finite elements in non-linear elasticity. *International Journal for Numerical Methods in Engineering.* 1999;44:1617-1652.

[47] Reese S., Wriggers P., Reddy B. D.. A new locking-free brick element technique for large deformation problems in elasticity. *Computers and Structures.* 2000;75:291-304.

[48] Sze K. Y., Liu X. H., Lo S. H.. Popular benchmark problems for geometric nonlinear analysis of shells. *Finite Elements in Analysis and Design.* 2004;40:1551-1569.

[49] Belytschko T., Lin J. I., Tsay C-S.. Explicit algorithms for the nonlinear dynamics of shells. *Computer Methods in Applied Mechanics and Engineering.* 1984;42:225-251.

[50] Benson D. J., Bazilevs Y., Hsu M. C., Hughes T. J. R.. Isogeometric shell analysis: The Reissner-Mindlin shell. *Computer Methods in Applied Mechanics and Engineering.* 2010;199:276-289.